JOURNAL OF GEOPHYSICAL RESEARCH, VOL. ???, XXXX, DOI:10.1002/,

An experimental investigation of acceleration-skewed oscillatory flow over vortex ripples

Jing Yuan[1], Dongxu Wang[1]

Plain Language Summary

In shallow coastal regions, shoaling waves produce oscillatory bottom flows, which create sand ripples on a sandy seabed. The acceleration skewness of the oscillatory flow is a result of the nonlinear feature of the overlying water waves, and it can differentiate the two half-cycles of the oscillatory flow and therefore leading to a net (cycle-averaged) sediment transport. In this study, we use an oscillatory water tunnel and particle image velocimetry to investigate the oscillatory boundary layer flow over vortex ripples with a focus on the effect of acceleration skewness. Our measurements provide detailed descriptions of the formation-ejection process of coherent vortices, which is produced by the flow separation behind the ripple crest. Some useful observations on flow turbulence are also provided. The results showed that acceleration skewness can substantially differentiate the two coherent vortices developed within the two half cycles. The offshore-side vortex can carry more turbulence over the ripple crest than the onshore-side vortex, which possibly leads to some net onshore sediment transport rate. We also showed that the ripple-averaged flow is fairly close to that over a flat bed, so flat-bed boundary layer model can be possibly used for rippled bed with some parameterizations.

---

[1] Department of Civil and Environmental

Key Points.

- A full-scale experimental study of acceleration-skewed oscillatory flow over 2-dimensional vortex ripples.
- Acceleration skewness differentiates the two coherent vortices within a flow cycle.
- The offshore vortex moves more residual turbulence across the ripple crest than the onshore vortex does.

Abstract. A full-scale experimental study of acceleration-skewed oscillatory flow over vortex ripples, which is an approximation of wave-driven flow over a rippled seabed, was conducted in an oscillatory water tunnel. Three acceleration-skewed-flow tests and a reference sinusoidal-flow tests were involved in this study. In each test, 2-dimensional vortex ripples were generated from a coarse-sand movable bed, and the flow field was measured with a particle image velocimetry. The dominant feature of phase-averaged flow is the generation of onshore (offshore) coherent vortices during the onshore (offshore) half-cycle. The acceleration skewness expedites the offshore-onshore flow reversal and therefore speeds up the ejection of offshore vortex, while the opposite occurs for the onshore vortex. The ripple-averaged flow is similar to the acceleration-skewed turbulent oscillatory flow over a flat bed in terms of leading Fourier harmonics, boundary layer thickness and cycle-averaged flow, suggesting a possible analogy between the two. From the aspect of flow

---

Engineering, National University of

Singapore, Singapore

turbulence, acceleration skewness elongates the offshore accelerating quarter, so the turbulence embedded in the offshore vortex can be better developed. This, together with a quick ejection process, allows the offshore vortex to carry a significant amount of residual turbulence to the onshore-side ripple flank, which may even enhances the production of turbulence within the onshore half-cycle. Some results on pressure field and form drag are also presented in this paper.

1. Introduction

Sandy seabeds in shallow coastal regions are often covered by sand ripples, which are generated by the oscillatory boundary layer flows under shoaling water waves. The dimension of sand ripples depends on flow and sediment conditions [see *Bagnold*, 1946; *Wiberg and Harris*, 1994; *O'Donoghue et al.*, 2006; *Pedocchi and García*, 2009], and is usually O(10∼100 cm) in length and O(1∼10 cm) in height. If the ratio of ripple height to length is sufficiently large (e.g., exceeds 0.1), the boundary layer flow can separate from the ripple surface after passing the ripple crest, which gives rise to coherent lee-side vortices. These coherent vortices are subsequently ejected into higher levels and washed over the ripple crest as the overlying oscillatory flow reverses. *Bagnold* [1946] named the steep ripples which can trigger significant coherent vortices as vortex ripples. The presence of vortex ripples has significant influences on many coastal processes, including dissipation of wave energy [e.g. *Tunstall and Inman*, 1975; *Nielsen*, 1983] and sediment transport [e.g. *Sato and Horikawa*, 1986; *van der Werf et al.*, 2006; *Hurther and Thorne*, 2011]. Thus, it is of interest to have a detailed understanding of the related hydrodynamic processes.

A considerable amount of knowledge regarding flow over vortex ripples has been obtained through controllable laboratory experiments. More than a century ago, *Darwin* [1883] and *Ayrton* [1910] were among the first to visualize coherent vortices using dye-injection techniques, but it is comparatively recently that detailed flow measurements became available for more quantitative investigations. A few studies with fixed or artificial ripples [e.g. *Tunstall and Inman*, 1975; *Earnshaw and Greated*, 1998; *Sand Jespersen et al.*, 2004] were aimed at understanding the dynamics of coherent vortices through obtaining the temporal-spatial variation of vorticity field. *Earnshaw and Greated* [1998] described the life-cycle of a vortex by its circulation, core location and a characteristic radius. They showed that the coherent vortex starts to grow since the beginning of a half-cycle and reaches its maximum strength around the phase of peak free-stream velocity. During the decelerating stage of a half-cycle, the vortex is moved towards the ripple crest while decaying. It is subsequently carried over the ripple crest shortly after the flow reversal and drifted with the reversed ambient flow until vanishing. *Nichols and Foster* [2007] used the evolution of swirling length to depict coherent vortex generated over an irregularly rippled bed in a full-scale wave-flume experiment, which allows them to discuss how flow characteristics and ripple geometry affect vortex generation and ejection.

The flow over vortex ripples is usually turbulent under field conditions, so it is of interest to separate the instantaneous flow field into phase-averaged flow, of which the spatial variation is controlled by the bottom topography, and small-scale turbulence, which appears "random" comparing to the phase-averaged flow. The phase-averaged flow, which includes the coherent vortex motion, is believed to play a dominant role in mixing sediment and momentum near the ripple surface. The flow turbulence, although playing a secondary role, also contributes to the sediment suspension. Some experimental studies were aimed at the turbulent dynamics. *Sato et al.* [1984] followed by *Sato et al.* [1987] reported experiments in an oscillatory water tunnel (OWT), in which oscillatory flows were produced over fixed ripples. They provided turbulence statistics, including turbulence kinematic energy, Reynolds stress and shear production. In some other experiments, e.g., *Toit and Sleath* [1981], *Fredsøe et al.* [1999] and *Hurther and Thorne* [2011], some results on turbulence statistics were also reported. Recently, *Hare et al.* [2014] conducted an oscillating-rig test with real vortex ripple and presented some detailed turbulence statistics. In all these studies, it is found that the coherent vortex contains much higher turbulence intensity than the ambient flow when it is growing in the lee side. As the lee vortex is ejected and moved to the other side of ripple crest, the embedded turbulence also moves with it until being dissipated and diffused into background turbulence. Thus, vortex shedding is important for the spatial and temporal variations of flow turbulence, as well as the associated physical processes, e.g., turbulent diffusion of sediment.

The presence of lee vortices reduces the local water pressure, so a ripple-averaged net streamwise pressure force (or form drag) is produced, which is the main contributor to the flow resistance. Some early studies attempted to estimate the flow resistance from flow energy dissipation [e.g. *Mathisen*, 1989; *Carstens et al.*, 1969] or the water pressure for driving the oscillatory flow [e.g. *Lofquist*, 1986; *Yuan and Wang*, 2018]. *Rankin and Hires* [2000] used shear-plate technique to directly measure the flow resistance. However, there is little work that links flow resistance to coherent vortex motions. By combining Particle Image Velocimetry (PIV) measurements of flow fields and pressure-based measurements of flow resistance, *Yuan and Wang* [2018] recently showed that the multiple peaks in the time variation of flow resistance occur at some key instances of vortex dynamics, e.g., when the free-stream velocity reaches its maximum and when the ejected vortex passes the ‘parent’ ripple crest.

In parallel with experimental studies, a number of numerical or theoretical works have been performed to simulate oscillatory flows over vortex ripples. Many of them are two-dimensional models that assume homogeneity in the horizontal transverse direction. The discrete vortex method, which has the relative ease for describing the generation-ejection processes of vortices, was adopted in many early works, e.g., *Longuet-Higgins* [1981], *Sleath* [1982], and *Malarkey and Davies* [2002]. This method, however, is inadequate for representing flow turbulence. Alternatively, some modellers solved the Reynolds-averaged flow with the aid of various turbulence-closure models, such as the $k-\epsilon$ model [e.g. *Sato et al.*, 1986] and the $k-\omega$ model [e.g. *Fredsøe et al.*, 1999; *van der Werf et al.*, 2008]. There are also some attempts using the Large-Eddy-Simulation (LES) technique [e.g. *Zedler and Street*, 2006; *Grigoriadis et al.*, 2012] or even Direct numerical simulation(DNS) [e.g. *Scandura et al.*, 2000; *Blondeaux et al.*, 2004; *Önder and Yuan*, 2019].

It should be pointed out that many previous studies deal with sinusoidal flows or artificial ripples, which are oversimplified for understanding wave-driven sediment transport over vortex ripples. In shallow coastal regions, nonlinear shoaling waves become skewed (flat trough but sharp crest) and forward-leaning, which leads to two features, i.e., velocity skewness and acceleration skewness, in the near-bed oscillatory flows [e.g. *Elfrink et al.*, 2006]. Velocity skewness makes the onshore half-cycle shorter than the offshore half-cycle but has a larger peak value, while acceleration skewness leads to a sawtooth-shaped time series of free-stream velocity, so the onshore velocity increases in magnitude faster than the offshore velocity. A number of experimental and theoretical studies have been conducted to understand how velocity and acceleration skewness differentiate the boundary layer flows within the two halves of a wave cycle [e.g. *van der A et al.*, 2011; *Yuan and Madsen*, 2015] and therefore produce net (cycle-averaged) sediment transport rate [e.g. *Ribberink and Al-Salem*, 1995; *O'Donoghue and Wright*, 2004; *van der A et al.*, 2010] over a flat bed, but there is little work in the vortex-ripple regime. Note that both velocity and acceleration skewness of oscillatory flow can change the ripple shape, which in turn alters the boundary layer flow, so experiments with real vortex ripples are more desirable than those with artificial ripples. *Sato and Horikawa* [1986] reported a small-scale OWT study, in which velocity-skewed oscillatory flows generated vortex ripples. They observed that the velocity skewness makes the onshore-side ripple flank steeper than the offshore side. Note that the onshore half-cycle also has a larger peak value of free-stream velocity, so the lee-side vortex developed in the onshore half-cycle is much stronger than that developed in the offshore half-cycle. As a result, the ejected onshore-side vortex is able to carry a substantial amount of sediment to the offshore ripple flank, which is not achievable by the much weaker offshore-side vortex. This mechanism leads to a net offshore sediment transport rate [cf. *Sato*, 1986]. *van der Werf et al.* [2007] reported a similar OWT study with velocity-skewed oscillatory flows, but their test conditions were full-scale. They provided detailed intra-cycle and intra-ripple variations of phase-averaged flow and sediment concentration, which allows them to experimentally investigate the sediment flux field and assess the influence of coherent vortex motion. These studies are focused on sediment transport processes, so less attention is paid to hydrodynamics. To the authors' knowledge, there is no comprehensive experimental study for acceleration-skewed oscillatory flows over vortex ripples, especially for full-scale conditions. This knowledge gap motivates the present study.

In this paper, we report a full-scale experimental study of acceleration-skewed oscillatory flow over 2-dimensional vortex ripples. The experiments were conducted in a large oscillatory water tunnel, and a PIV system was deployed to obtain flow measurements. The objective is to understand how acceleration skewness affects various aspects of the oscillatory boundary layer flow over vortex ripples, which can provide insights for understanding sediment transport. The paper outline is as follows. The experimental setup and procedure are presented in section 2. Section 3 presents the phase-averaged velocity with an emphasis on coherent vortex motions. Some discussions on the intensity of turbulence are provided in section 4. Pressure fields and form drag estimated from flow measurements are presented in section 5. Section 6 provides conclusions.

2. Experimental setup

2.1. Experimental facility and instrumentation

The main research facility is an oscillatory water tunnel at the hydraulic lab of National University of Singapore. As shown in figure 1, this facility has a 10-m-long horizontal tunnel with a 40-cm-wide and 50-cm-deep working cross section. Honeycomb flow filters connect the ends of the tunnel to vertical cylindrical risers. One riser is open to the air, and the other riser contains a hydraulic-driven piston. The whole facility is filled with water, so a vertical oscillation of the piston is translated into a horizontal oscillatory flow in the test channel, which is up to 2 m/s and 2 m/s^2 in velocity and acceleration, respectively. A few previous studies have demonstrated that the facility can accurately produce a target oscillatory flow with a variety of wave shape [see *Yuan and Madsen*, 2014]. Thus, the facility can provide full-scale approximation of wave-driven near-bed flows. A 9m-long and 20-cm deep trough is attached to the bottom of the test channel for holding sediments, so this facility can be used for studying sediment transport under oscillatory flows [e.g. *Yuan et al.*, 2017; *Wang and Yuan*, 2018].

A 2-dimensional PIV system supplied by the TSI Corporation was deployed to measure the flow field over a vortex ripple. As shown in figure 1, the viewing window was located around the longitudinal center of the test channel. To illuminate the flow field, a doublepulsed YAG 135-15 Litron Nano L laser produced a thin laser sheet, which was introduced into the test section vertically downward through the transparent lid. The laser sheet was carefully aligned with the longitudinal direction of the test channel and was positioned about 10-cm from the sidewall. For each sampling, a high-speed Powerview 4M Plus camera (2000-by-2000 pixel) is used to capture an image pair of the illuminated flow field with a very short time interval ($\sim$ O(1000 μs)), so a 2D field of velocity vectors can be obtained by a cross-correlation analysis (through the TSI's Insight 4G software) of the image pair. More details about the PIV setup will be introduced in conjunction with the experimental procedure in section 2.3.

2.2. Test conditions

In this study we focused on periodic oscillatory flows, and acceleration skewness is introduced into the free-stream velocity, $u_\infty(t)$, by adding a second harmonic to the basic sinusoidal oscillatory flow, i.e.,

$$u_\infty(t) = U_{\infty,1}\cos(\omega t) + U_{\infty,2}\cos(2\omega t + \Phi_{\infty,2}) \tag{1}$$

where $U_{\infty,1}$ and $U_{\infty,2}$ are the 1st- and 2nd-harmonic-velocity amplitudes, respectively, $\omega = 2\pi/T$ is the radian frequency, and Φ_2 is the second-harmonic phase with a target value of 90°. Totally four tests with different flow conditions were performed in this paper, and table 1 presents the actual values of the $U_{\infty,1}$, $\alpha_2 = U_{\infty,2}/U_{\infty,1}$ and Φ_2 obtained by Fourier analyzing the measured free-stream velocity. All tests have the same flow period, T, of 6.25 s. The primary test, ASY60a, which will be used as the main test for discussions, has a $U_{\infty,1}$ about 57 cm/s and a α_2 about 0.27. The second test, ASY45a, has the same wave shape (determined by α_2 and Φ_2) as ASY60a but a smaller $U_{\infty,1}$ (about 45 cm/s).

The third test, ASY60b, has the same $U_{\infty,1}$ as ASY60a but a less acceleration-skewed wave shape (α_2-value is reduced to 0.14). The last test, SIN60, is a sinusoidal-flow test with a $U_{\infty,1}$ very close to that of ASY60a and ASY60b, and it will be taken as a reference to illustrate the effect of acceleration skewness. The Reynolds number, which is defined as $Re = U_{\infty,1}A_{\infty,1}/\nu$ (here $A_{\infty,1} = U_{\infty,1}/\omega$), is of the order 10^5, so all tests are full-scale. The positive flow direction is also the positive x-direction (towards the piston end) of the test channel (see figure 1), which will be referred to as the onshore direction in the following text.

The four tests were conducted with the same movable sand bed, which is made of uniform coarse sand with a median diameter d_{50} of 0.51 mm. This sand has a geometric standard deviation, $\sigma_g = 0.5(d_{84}/d_{50} + d_{50}/d_{16})$, of 1.43, where d_{84} and d_{16} are particle diameters for which 84% and 16%, respectively, of the sediment sample are finer. Using coarse sand is primarily because some previous studies showed that this grain size can lead to 2-dimensional vortex ripples [see *Wang and Yuan*, 2018], while our PIV system can only provide 2-dimensional flow measurements. For each test, sand ripples were first developed from the movable bed by running the test for about 30-80 minutes, and we indeed had 2-dimensional equilibrium ripples for all test conditions. The ripple profile was obtained by analyzing PIV images, which will be introduced in the next sub-section. Unlike the onshore-leaning ripples developed under velocity-skewed oscillatory flows, the ripples in our three acceleration-skewed-flow tests are quite symmetric regarding the vertical line through the ripple crest. The four tests have quite similar ripple dimensions (see table 1). The ripple height, η, is about 10 cm, and the ripple length, λ, is about 60 cm. Many previous studies have shown that the normalized ripple length $\lambda/A_{\infty,1}$ decreases with the mobility number $\Psi = U_{\infty,1}^2/[(s-1)gd_{50}]$, where $s \approx 2.65$ is the sediment specific density and g is gravitational acceleration. Thus, it is not surprising that test ASY45a has similar ripple dimensions as the rest three tests. The ripple steepness, η/λ, is within 0.16∼0.20, so the obtained ripples are steep enough for triggering flow separation. Except for the sinusoidal-flow test, ripples migrated very slowly in the onshore direction with a speed of O(0.1 mm/s) (see the last column of table 1).

2.3. Experimental procedure and preliminary data analysis

Our target is to measure the 2D flow field covering a whole vortex ripple, which is about 60 cm long and migrates onshore. The boundary layer flow over vortex ripples can be extended to 2-3 ripple height (or 20∼30 cm) above the ripple crest. Thus, the whole domain should be about 60 cm wide and 30∼40 cm deep. Such a large domain was covered by two viewing windows with each window containing one half ripple. For the sinusoidal-flow test, SIN60, the symmetries of flow and ripple shape allow us to only measure the flow over a half-ripple and mirror the measurements to cover the other half, so the size of viewing window was chosen to be 37 cm-by-37 cm, which has a spatial resolution of 3.3 mm. The readers are referred to *Yuan and Wang* [2018] for details about the mirroring. For the rest three tests, the ripples migrated onshore. To ensure that a half-ripple is covered throughout a continuous PIV burst, the viewing window was made slightly larger, i.e., 44 cm-by-44 cm, which gives a spatial resolution of 3.9 mm. Note that instead of moving the PIV camera, we utilized the ripple migration to ‘move’ the viewing window. Each PIV burst covered 32 flow cycles for phase-averaging, and the sampling frequency was set to 5.12 Hz, which gives 32 samples per flow cycle (note that T=6.25 s for all tests). We found that having 32 flow cycles is sufficient for the convergence of phase-averaged flow and turbulence statistics, because the results would only change a little if the analysis was based on 16 flow cycles. It is impractical to separate suspended sand grains out in the PIV analysis, since the local sediment concentration can be quite high near the ripple surface and within the coherent vortices. Thus, we have to treat the suspended sediment grains as seeding particles, and the PIV more-or-less measured the particle velocity rather than the fluid velocity in the region where high sediment concentration occurs. The inertia of our sediment grains may not be negligible due to their relatively large size (d_{50}=0.51 mm), so it is possible that particle velocity deviates from the local flow velocity. Some discussions and a correction of PIV measurements will be introduced in the next subsection.

The ripple profile was obtained by analyzing the PIV images as follows. The PIV laser sheet produces a thin laser line on the ripple surface, which appears in the images as a narrow strip with very high brightness values. Therefore, the ripple surface can be determined by locating the peak brightness value within this strip. It is impossible to resolve the ripple surface frame-by-frame, because at certain phases the laser is mostly reflected by the dense sediment-laden vortices, so there is no clear laser line on the ripple surface. Alternatively, the whole set of PIV images was first ensemble-averaged, which took the ripple migration into consideration. In the derived image a narrow and bright strip following the ripple surface was always present, allowing the detection of bottom profile. This analysis was performed for both viewing windows of a test, and the two bottom profiles were combined to give a global ripple profile. More details are presented in the supporting information S1. It should be noted that the ripples slightly changed shape during a flow cycle. Thus, the obtained ripple profile should be interpreted as a cycle-averaged ripple profile, and the instantaneous rippled bed may deviate from it by a few mm. This must be considered when interpreting the measurements very close to the ripple surface.

The ripples migrated by a few centimetres during a continuous PIV measurement (32 flow cycles), so an adjustment of x (horizontal) coordinate and some interpolation of velocity vectors were performed frame-by-frame for later phase-averaging. Here, the $x-z$ coordinate of the first PIV frame was taken as a reference with the origin ($x = 0$, $z = 0$) set at the ripple crest. For the subsequent PIV frames, the z-coordinate remained unchanged since the ripple only moved horizontally, but the local horizontal coordinate x' was converted to the reference x-coordinate through $x_{adj} = x' - c_b t$. The PIV vectors within the region, $0 < x_{adj} < L - c_b NT$, where L is the physical width of viewing window, N is the number of flow cycles and c_b is the ripple migration speed (see the supporting information S1 for the determination of c_b), were interpolated onto a reference grid $[x_i]$-$[z_j]$, which is the grid of the first PIV frame. With this adjustment, phase averaging of a physical variable ξ can be easily calculated, i.e.,

$$\tilde{\xi}(x, z, t) = \frac{1}{N} \sum_{n=1}^{N} \xi(x, z, t + (n-1)T) \tag{2}$$

The two components (u or w) of PIV vectors were first phase-averaged. For brevity, the tilde sign, which indicates phase-averaging, will be neglected hereafter. The free-stream velocity, u_∞, was obtained by averaging u at the top z-level, which was Fourier analyzed to give the leading two harmonics in table 1. A phase-coordinate, $\theta = \omega t$, which makes the phase of the first harmonic of u_∞ zero, as in equation (1), was then assigned to the phase-averaged frames of a flow cycle. The turbulent fluctuations (u' and w') were obtained by subtracting the phase-averaged velocity from the instantaneous velocity. A turbulence intensity associated with u' and w' was introduced as

$$e_{ti} = \frac{\widetilde{u'^2} + \widetilde{w'^2}}{2} \tag{3}$$

To combine measurements from the two viewing windows, a global grid for each test was established as follows. Note that the PIV camera remained untouched during a test, the same z-grid applied for both viewing windows, and therefore was simply taken as the global z-grid. A phase (θ)-grid from $\theta = 0$ to 2π was introduced with a phase step of $\Delta\theta = \pi/16$, which simply follows the temporal resolution of PIV measurements. The global x-grid was set to have a spacing equal to the horizontal resolution of PIV measurements. The measurements from each viewing window were first interpolated onto the global x-grid, and then interpolated onto the global θ-grid. A weighted average was applied in the region covered by both viewing windows. Two ripple troughs on the two sides of ripple crest were located from the global bottom profile, and measurements outside the two troughs were trimmed off, so a field covering a whole ripple was obtained eventually.

2.4. Fidelity of PIV measurements

The particle velocity deviates from the fluid velocity, if the inertia of the particle is not negligible. This deviation must be considered for evaluating whether the particles can provide a good tracking of the flow. For instance, *Maxey and Corrsin* [1986] showed that particles in vortex flows get concentrated on particular paths and hence sample the fluid velocity field with a bias. In a still water (or no flow acceleration), the relative velocity between sand and water is the still water settling velocity w_s. Using the formula of *Jiménez and Madsen* [2003], w_s is estimated to be 6.5 cm/s for the sand grains used in this study (d_{50}=0.51 mm), which is apparently non-negligible. When the flow acceleration is much smaller than the acceleration of gravity, *Nielsen* [1992] showed that the additional relative velocity (actual relative velocity minus w_s) is of the order (ϵw_s), where ϵ is $|du/dt|/g$. A key objective of this paper is to investigate the phase-averaged flow, which includes the coherent vortex. The characteristics acceleration is $U_{\infty,1}\omega$, which is about 4-6% of the acceleration of gravity. Thus, for phase-averaged flow the additional relative velocity can be considered negligible comparing to w_s.

The correction of phase-averaged flow (to remove the bias due to settling velocity) is as follows. It should be noted that there are also lots of very fine particles (e.g., the dust contained in the sand bed) suspended in the water column. In fact they are the main seeding agent at high levels, where the sand concentration is very low. In a PIV interrogation grid, there are both sand grains and very fine particles, and the algorithm treats them equally. As a result, the “apparent” settling velocity (or the mean settling velocity of all particles in an interrogation grid) reduces with the sediment concentration. Thus, it is not reasonable to simply subtract the w_s of sand grains from the PIV measurements. For instance, this would introduce a huge bias in the free-stream region, where very few sand grains can reach. On the other hand, it is impossible to determine a detailed spatial variation of apparent settling velocity for each phase, since we do not have the information on sediment concentration. As a compromise, we followed the method proposed by *van der Werf et al.* [2008]. For each phase of the phase-averaged flow, the 2D field of vertical velocity is ripple-averaged into a profile of vertical velocity, $< w > (z,t)$ (see section 3.2 for details about ripple averaging). The obtained $< w > (z,t)$ decreases towards the higher levels and almost vanishes in the free stream, which is mainly because the main seeding agent changes from sand grain in the near-bed region to dust at higher levels. Also,

$< w > (z,t)$ is around 5-7 cm/s below the ripple crest, which is in agreement with w_s=6.5 cm/s. Phase-by-phase, the profile of $< w > (z,t)$ was calculated and subtracted from the 2D phase-averaged flow field. A merit of this correction is that the ripple- and phase-averaged vertical velocity is made zero after the correction, which satisfies the principle of volume conservation. In other words, the correction removes the vertical variation of the "apparent" settling velocity (which should be the main direction of spatial variation), as well as the temporal variation (the correction is phase-by-phase). However, the horizontal variation of the "apparent" settling velocity (due to a horizontal variation of sediment concentration) is not removed, but this variation should be secondary comparing to the vertical and temporal variations. Thus, the corrected phase-averaged flow measurements (to be discussed in section 3 and 5) should be sufficiently accurate.

The bias due to settling velocity has a minor effect on turbulence statistics, because it is mostly removed when calculating the turbulence fluctuations by subtracting the phase-averaged velocity from the instantaneous velocity. There are, however, some other critical issues that limit the accuracy of turbulence statistics. To see whether the sand particles can loyally trace the small-scale turbulence, we consider the particle relaxation time, i.e., the time for a particle to accelerate to a new surrounding velocity, which is given by $\tau_r = (s-1)d^2/18\nu$, where $s = 2.65$ is the sediment specific density, ν is the water kinematic viscosity and d is the particle diameter. For our sediment grains (d_{50}=0.51 mm), the relaxation time is 0.02 s. Note that this estimate of τ_r requires a very small particle for the applicability of the Stokes' law, which gives the drag force on a spherical particle. For larger particles, like the sand grains in our study, Stokes' law will underestimate the drag force, so the estimate of τ_r here is conservative. Small-scale flow structures with a time scale less than τ_r is not resolvable due to the inertial of the sediment grains. Indeed, many previous studies [e.g. *Snyder and Lumley*, 1971; *Nielsen*, 2009] have shown that the particle velocity variance can be smaller than the fluid velocity variance (i.e., the small-scale turbulence). It should also be noted that the size of PIV interrogation grid (i.e., the spatial resolution) is about 3-4 mm, so some small-scale turbulence is already filtered out by the averaging nature of PIV analysis. Thus, using sand grains as seeding particles matches the PIV setup. The key flow structure, i.e., the coherent vortices, is quite large (a spatial scale of a few cm and a time scale of a few seconds), and therefore can be well captured by the PIV setup and using sand grains as tracing particles, but flow turbulence may not be resolved with high fidelity. Following *Pope* [2000], we estimate that the energy-containing eddies in our tests roughly have length scales of 1-10 cm, so our PIV can more-or-less resolve these large eddies, but surely misses any smaller eddies. Another issue to be noted is that sediment concentration varies with time and space in our tests. As mentioned before, we treat sand grains and very fine particles (mainly dust) equally as seeding particles. Thus, the PIV's ability in resolving turbulence changes with local sediment concentration, e.g., the small-scale turbulence may be better resolved when the local sediment concentration is low. Nevertheless, this effect should be secondary, because its influence is mainly on resolving very small-scale turbulence, which is already prevented by the size of PIV interrogation grid. Based on these discussions, we must acknowledge that the turbulence statistics obtained in this study is rather qualitative.

The suspended sand grains reduce the fidelity of our PIV measurements, which is the main drawback of our study. However, doing experiments in such a way allows loyally capturing the flow-sediment interaction, which is an intrinsic process of this type of boundary layer flow. Many previous studies on sediment-laden flows in steady unidirectional flows [e.g. *Einstein and Chien*, 1955; *Styles and Glenn*, 2000; *Herrmann and Madsen*, 2007] showed that the effect of stratification due to suspended sand on flow velocity can be very significant. For instance, stratification (or large concentration gradient) leads to the damping of turbulence within the boundary layer, which modifies the Reynolds-averaged flow and sediment concentration. It is reasonable to believe that similar flow-sediment interaction will exist for oscillatory flows over vortex ripples. Thus, collecting PIV measurements over a real movable bed helps to ensure that our observations can be directly applied for understanding the sediment transport process.

3. Phase-averaged flow

In this section we first present the phase-averaged velocity fields with an emphasis on the coherent vortex motions. Some results regarding ripple-averaged flows will also be presented.

3.1. Coherent vortex motions

To reveal the coherent vortices, the spanwise vorticity is calculated from the phase-averaged velocity and normalized by the radian frequency, i.e.,

$$\Omega^* = \frac{\Omega}{\omega} = \frac{1}{\omega}\left(\frac{\partial w}{\partial x} - \frac{\partial u}{\partial z}\right) \tag{4}$$

Vorticity cannot always give a satisfactory identification of the region with strong swirling motions if the ambient shear is strong. Alternatively, *Nichols and Foster* [2007] used the swirling length criterion proposed by *Zhou et al.* [1999] for vortex identification in their rippled-bed experiments. For two-dimensional flow, the swirling length, Λ_i, is the imaginary part of the complex conjugate eigenvalue of the velocity gradient tensor D:

$$D = \begin{bmatrix} \partial u/\partial x & \partial u/\partial z \\ \partial w/\partial x & \partial w/\partial z \end{bmatrix} \tag{5}$$

Higher value of Λ_i indicates stronger swirling motion. Its physical meaning is a measure of local twisting rate within a vortex [cf. *Chakraborty et al.*, 2005], so it can better differentiate the vortex from the background shear flow. In the following discussions we shall use Ω^* in conjunction with the contours of normalized swirling length $\Lambda_i^* = \Lambda_i/\omega = 1$ to identify the coherent vortices. Here choosing $\Lambda_i^* = 1$ as a threshold is because the associated contours can nicely outline the vortices.

Figure 2 presents the fields of phase-averaged velocity (vectors), Ω^* (shades) and contours of $\Lambda_i^* = 1$ for test ASY60a at a few selected phases across a flow cycle. To reduce the data noise, both Ω^* and Λ_i^* are smoothed by calculating the moving average of a 5-by-5 window around each grid point. The first key phase (figure 2b) is when the onshore free-stream velocity reaches its peak value. On the offshore (left)-side ripple flank, the boundary layer flow is attached, and the near-surface flow is forced to accelerate towards the ripple crest due to the rise up of ripple surface, so the instantaneous flow above the ripple crest has a larger magnitude than the free-stream velocity. In the onshore or lee side, flow separation occurs, and the flow is reversed within a thin layer near the ripple surface. A lee vortex with strong negative vorticity occupies the region from ripple crest to more than halfway between the crest and the trough, which is enclosed by the $\Lambda_i^* = 1$ contours. The flux of negative vorticity passing the ripple crest feeds the lee vortex, so it continues to grow as the flow decelerates. As shown in figure 2 c and d, the lee vortex grows in size, e.g., at $\theta = 33.75°$ the area enclosed by $\Lambda_i^* = 1$ contours is extended onshore to the ripple trough and upward to about $z/\eta = 0.5$ above the ripple crest. The flow separation also becomes much more significant in the lee side. Note that the big 'head' of the negative-vorticity region, where a circulation is formed by the separated flow, is isolated by a closed $\Lambda_i^* = 1$ contour. This region has very high Λ_i^*, indicating a strong swirling motion, while the separated shear layer from the ripple crest, which is like a 'tail' connecting the big 'head' to the ripple crest, has much lower Λ_i^*, since the local vorticity is mainly due to the high local shear. This shows that Λ_i^*-criterion can indeed better identify the coherent vortices. Beneath the primary negative lee vortex there is a secondary vortex with positive vorticity that also develops with time. This phenomenon was documented by the numerical modelling of *Blondeaux and Vittori* [1991] and recently confirmed by the DNS work of *Önder and Yuan* [2019]. This secondary vortex is produced by the adverse pressure gradient along the ripple surface, and it forms a vortex dipole with the primary vortex. Around the phase when u_∞ is about to reverse, the primary lee vortex begins to eject itself from the ripple surface. Figure 2e shows the phase $\theta = 80.4°$ when u_∞ is reduced to zero. The vortex dipole creates a very strong near-surface flow towards the ripple crest on the onshore (right) ripple flank, and this flow in turn carries the vortices towards the ripple crest. Based on the magnitude of vorticity, it is clear that the strength of vortex has been reduced a lot. Shortly into the offshore half-cycle, i.e., $\theta = 127.1°$ in figure 2f, the negative primary vortex reaches the ripple crest. The Λ_i^*=1 contours outline a few little patches of negative vorticity above the ripple crest, suggesting that the primary vortex has low coherency at this moment. The positive secondary vortex now covers the ripple crest. As the offshore free-stream velocity continues to accelerate, e.g., $\theta = 164.8°$, the weak primary vortex is moved further offshore by the ambient flow until becoming background turbulence. The secondary vortex moves to the offshore side of ripple crest and grows into a new primary lee vortex in the offshore side, of which the remaining life cycle is depicted in figure 2h-m. Hereafter we shall refer to the primary vortex developed on the onshore (offshore) lee side as the onshore (offshore) vortex.

Some observations that reflect the effect of acceleration skewness are as follows. First of all, acceleration skewness affects the required time for the ejected primary vortex to reach the parent ripple crest. From figure 2 e and f, the ejected onshore vortex takes about 47° in phase to move to the ripple crest, while it only takes about 23° in phase for the ejected offshore vortex (figure 2 k and i) to reach the crest. This is because the onshore vortex is mostly carried by the near-bed flow produced by itself, since the relatively lower $|du_\infty/dt|$ makes the ambient flow velocity increase slowly after the onshore-offshore reversal. The opposite occurs for the offshore vortex, i.e., the relatively high $|du_\infty/dt|$ produces a noticeable ambient flow after the offshore-onshore reversal, which helps to move the offshore vortex (note the difference in the ambient flow between figure 2 f and l). When arriving at the ripple crest, the offshore vortex seems to be stronger than the onshore vortex, as can be seen by comparing the area enclosed by the Λ_i^*=1 contours in figure 2 f and l. This is mainly because the offshore vortex has a shorter residence time within the lee side, and therefore is less dissipated by flow turbulence.

To better illustrate how acceleration skewness differentiates the life cycles of onshore and offshore vortices, we calculated the location of vortex core and the strength of vortex as follows. Since we have shown that Λ_i-criterion can better capture the region with strong swirling motion, we defined the onshore/offshore coherent vortex as where the vorticity is negative/positive and $\Lambda_i^* > 1$, and identify the regions, A_+ and A_-, occupied by the onshore and the offshore vortices, respectively. The strength of the onshore vortex (normalized by η^2) is represented by the integral of Λ_i^* over A_+, i.e.,

$$I_{\Lambda+} = \frac{1}{\eta^2} \int_{A_+} \Lambda_i^* dA \tag{6}$$

Likewise, an $I_{\Lambda-}$ is obtained for the offshore vortex. Note that a vortex is not identifiable when it is not born yet (e.g., no offshore vortex in figure 2b) or almost vanishes into ambient turbulence (e.g., no onshore vortex in figure 2h). This index essentially means that a vortex's strength depends on its size and the magnitude of swirling motion. The location (x_{c+}, z_{c+}) of onshore vortex core is given by

$$x_{c+} = \frac{\int_{A_+} \Lambda_i^* x dA}{\int_{A_+} \Lambda_i^* dA}, z_{c+} = \frac{\int_{A_+} \Lambda_i^* z dA}{\int_{A_+} \Lambda_i^* dA} \tag{7}$$

Likewise, the location of offshore vortex core (x_{c-}, z_{c-}) is also obtained.

Figure 3 presents the results for the two tests, ASY60a and ASY60b. The strength of both vortices (see figure 3 a1 and b1) increases during the accelerating stage of their half-cycle and peaks shortly after the phase of peak u_∞. For test ASY60a, the two phases of peak strength are already presented in figure 2 d ($\theta = 33.75°$) and j ($\theta = 247.50°$). The coherent vortices are fed by the flux of vorticity from the ripple crest when growing, but at these two phases the separated shear layer from the ripple crest produces rather weak vorticity. Therefore, the lee vortex cannot receive enough feeding to maintain its growth and starts to decay in strength. When u_∞ is reduced to zero, the strength of the vortex is about half of the peak value, and when the vortex is washed over the ripple crest, the strength is almost decayed to zero. These are in agreement with the vorticity fields shown in figure 2.

The x-coordinates of the vortex cores are presented in figure 3 a2 and b2 for the two selected tests. The trajectories of vortex cores are shown in figure 3 a3 and b3. For clarity the results are only shown for the phases after the vortices have reached their maximum strength. The x-coordinate allows us to estimate the residence time of a vortex in its born side, which is defined as the time from its maximum strength to when it passes the ripple crest (i.e., x_c=0). For test ASY60a (figure 3 a2) the onshore vortex has a residence time (in terms of phase angle θ) of about 93° (from $\theta = 33.75°$ to $\theta = 127.11°$), while the offshore vortex only has a residence time of about 48° (from $\theta = 247.50°$ to $\theta = 294.68°$). Thus, the offshore vortex has about 50% less resident time than the onshore vortex for this test, and the same applies for test ASY45a. For test ASY60b, the difference is smaller due to a lower acceleration skewness, i.e., 76° vs. 62° (onshore vs. offshore). Note that in the sinusoidal-flow test, SIN60, the residence time for a lee vortex is about 66°, so clearly the acceleration skewness reduces the residence time for the offshore vortex but increases the residence time for the onshore vortex. After passing the ripple crest, the offshore vortex can travel onshore by more than a half ripple length (0.5λ) before it becomes not identifiable, while the onshore vortex travels into the offshore side by a much shorter distance (less than 0.5λ) before vanishing. Note that in the sinusoidal-flow test, the ejected vortex vanishes at about 0.5λ from the crest. As has been discussed, offshore-onshore flow reversal has a larger $|du_\infty/dt|$ due to acceleration skewness, so the offshore vortex rides on a larger ambient flow after passing the ripple crest, and therefore travels further away from the ripple crest.

In summary, the most significant effect of acceleration skewness on vortex dynamics is that it expedites the ejection process of the offshore vortex and allows it to travel further into the onshore-side of ripple crest, while the opposite effect is experienced by the onshore vortex.

3.2. Ripple-averaged flows

Large-scale coastal modelling can only consider vortex ripples in a ripple-averaged sense, which allows applying existing theories on flat-bed boundary layers with certain parameterizations, e.g., a large bottom roughness. Here we briefly present some key observations of the ripple-averaged horizontal velocity. Spatial-averaging has been applied to study oscillatory flows over bottom covered by large roughness by many researchers. Here we follow *Giménez-Curto and Lera* [1996] and *Rodríguez-Abudo and Foster* [2014] to define a spatial-averaging of a physical quantity ξ at a vertical level z as

$$< \xi(z) >= \frac{1}{L_f} \int_{L_f} \xi(x,z) dx \tag{8}$$

where L_f denotes the width of the flow field covered by fluid. For $z > 0$ (above ripple crest), L_f is just the ripple length, so equation (8) is simply x-averaging ξ across a whole ripple, while below the ripple crest ($z < 0$), equation (8) means that the averaging is applied to the regions occupied by water.

The ripple-averaged horizontal velocity $< u >$ is Fourier analyzed, i.e.,

$$< u > (z,t) = Re \sum_{n=1}^{\infty} U_n(z) e^{i[n\omega t + \Phi_n(z)]} + < u_0 > \tag{9}$$

where $< u_0 >$ is the mean, $U_n(z)$ and $\Phi_n(z)$ are the amplitude and the phase of the n-th harmonic, respectively. The leading two harmonics are presented in figure 4 for the four tests. For test SIN60, only the first harmonic is presented. Note that very close to the ripple trough ($z/\eta \sim -1$) the results become unreliable since very few data points are available for averaging, so the presentations start from $z/\eta = -0.8$. The U_1-profiles exhibit a clear overshoot at the level slightly above the crest. It can be seen from the velocity field (e.g. figure 2) that the stoss-side flow is forced to accelerate as it approaches the ripple crest, which makes the ripple-averaged flow above the ripple crest stronger than the free-stream flow. Below the crest U_1 decreases towards the bottom. The first-harmonic phase Φ_1 generally increases towards the bottom in the region $z/\eta < 2$ (two ripple heights above the crest). It becomes about 10-20° at the crest level, and further increases to about 40° near the trough. This means that the flow below the ripple crest leads the free-stream flow in phase. As can be seen in figure 2 c-d, the flow separation in the lee side lets the near-surface flow reverse much earlier than the free-stream flow, so when the free-stream velocity is just decelerated to zero (e.g. figure 2e), the reversed near-surface flow in the lee side has already become quite strong. It should be noted that some researchers [e.g. *Nielsen*, 2016] have suggested that a depth-invariant turbulent eddy viscosity should be used in modelling the turbulent oscillatory boundary layer with a large bottom roughness. Such models predict a 45° phase lead of the near-bed flow velocity, which agrees quite well with our measurements. Overall speaking the behaviour of 1st-harmonic velocity is quite similar to that of flat-bed turbulent oscillatory flow [e.g. *Yuan and Madsen*, 2014], which also has an overshoot in U_1-profile and a positive Φ_1 that increases towards the bed. The second-harmonic velocity behaves similarly as the first-harmonic velocity. The overshoot of U_2 near ripple crest is more significant. The profiles of $\Phi_2 - \Phi_{\infty,2}$ are similar to the profiles of Φ_1.

A key effect of acceleration skewness on flat-bed turbulent oscillatory flows is that it decreases the time for boundary layer to be developed within the onshore half-cycle, and the opposite occurs for the offshore half-cycle. Therefore, the onshore half-cycle has a thinner boundary layer than the offshore half-cycle [e.g., *Nielsen*, 1992; *van der A et al.*, 2011]. To see whether this argument is applicable for the ripple-averaged flow, Figure

5 compares the velocity profiles at the phases of peak free-stream velocity. For an easy comparison, $< u >$ is normalized by $u_\infty(t)$. Here we located the level where local $< u >$ deviates from $u_\infty(t)$ by 3% as an indicator of boundary layer thickness, which are denoted by the circles in figure 5. For the three acceleration-skewed-flow tests, it can be clearly seen that the black circles are always below the red circles in figure 5 by a distance between 0.2η to 0.5η, suggesting that the instantaneous boundary layer at the phase of peak onshore velocity is thinner than that at the phase of peak offshore velocity. Comparing ASY60a and ASY60b (Figure 5 a vs. b), it is also found that the difference in boundary layer thickness is larger if the acceleration skewness is stronger. Thus, it appears that the effect of acceleration skewness on boundary layer thickness is similar for both ripple-averaged and flat-bed turbulent oscillatory flows.

Finally, we present the mean (cycle-averaged) ripple-averaged horizontal velocity, $< u_0 >$, in figure 6 for the three acceleration-skewed-flow tests. For test ASY60a, $< u_0 >$ is negative (or offshore) in the region below z/η=1.6, and the peak negative $< u_0 >$ is up to -4 cm/s and occurs at about 0.25η below the ripple crest. At high levels (i.e., $z/\eta > 1.6$) $< u_0 >$ becomes positive (or onshore). The same feature is present in the $< u_0 >$ of the other two tests, but the magnitude of $< u_0 >$ is smaller. Such a mean velocity profile is also observed in many flat-bed OWT studies with velocity- or acceleration-skewed oscillatory flows, e.g., *Ribberink and Al-Salem* [1995] and *van der A et al.* [2011]. For the flat-bed scenarios, velocity and acceleration skewness can produce a boundary layer streaming in the offshore (negative) direction, which is balanced by an onshore (positive) return current in an OWT [e.g. *Yuan and Madsen*, 2015]. To interpret the observed $< u_0 >$, we cycle-averaged the 2D flow field (u, w) and present the obtained mean velocity field for the four tests in figure 7. It can be seen that two counter-rotating mean circulations are located above the two ripple flanks. Similar observation was obtained in other OWT tests, e.g., *Nakato et al.* [1977]. They produce strong mean velocity close to the ripple surface, which conveys water towards the ripple crest. Such a mean circulation is also present for low-steepness ripples where no flow separation occurs [e.g. *Blondeaux*, 1990]. As a result of acceleration skewness, the mean flow right above the onshore-side ripple flank is stronger than that above the offshore-side ripple flank, as can be seen in figure 7 a-c. Apparently, ripple-averaging such a mean flow field gives a negative $< u_0 >$ at the levels around the ripple crest, as observed in figure 6. To balance the negative mean flow in the lower part of boundary layer, a positive return current must be produced by the facility, which gives the positive $< u_0 >$ at high levels. It should be mentioned that propagating waves will produce an boundary layer streaming in the onshore (here positive) direction, which was first illustrated by the analytical work of *Longuet-Higgins* [1953]. This boundary layer streaming may play a dominant role in the ripple- and time-averaged streamwise velocity, but OWT tests cannot capture this streaming due to the forced streamwise homogeneity.

These observations collectively suggest that there can be a reasonable analogy between the ripple-averaged oscillatory flows over vortex ripples and the flat-bed turbulent oscillatory boundary layer flows, as far as acceleration skewness is concerned.

4. Turbulence intensity

The motion of suspended sand grains over vortex ripples (e.g., entertainment and diffusion) is heavily controlled by the flow turbulence, so understanding the spatial-temporal variation of turbulent intensity can provide useful insights for understanding how acceleration skewness leads to a cycle-averaged sediment transport. The sinusoidal-flow test, SIN60, is taken as a reference, and we first present its results to provide some key background information. The acceleration-skewed-flow tests are then compared with the reference to demonstrate the effect of acceleration skewness. We would like to remind the readers again that our PIV setup cannot fully resolve flow turbulence. Nevertheless, the purpose here is to see the difference between the two half-cycles due to acceleration skewness, rather than providing solid measurements for any model benchmarking, so our results are adequate for this purpose.

4.1. The reference sinusoidal-flow test

We first look at the turbulence intensity, e_{ti}, of test SIN60, of which the free-stream velocity is $u_\infty = U_{\infty,1}\cos\theta$. figure 8 shows the snapshots of the e_{ti} fields. Since the two half-cycles of a sinusoidal oscillatory flow are symmetric, we just present 8 snapshots between $\theta = 0°$ and 180°. Overall, flow turbulence is concentrated within the coherent vortex (identified with the Λ_i^*=1 contours), as the vortex evolves and moves within its life cycle. A coherent vortex begins its life cycle around 30 $\sim$ 50° before the maximum free-stream velocity (e.g., figure 8i), and reaches its maximum strength about 30 $\sim$ 50° after the maximum free-stream velocity (e.g., figure 8d). During this period, the flow turbulence embedded within the coherent vortex increases, and the highest turbulence intensity (in terms of magnitude and spatial coverage) occurs around the phase of maximum vortex strength, e.g., $\theta = 45°$ (figure 8d). The DNS work of *Önder and Yuan* [2019] showed that shear production of turbulence mainly occurs within the separated shear layer in the immediate wake behind the ripple crest, where the local shear strain is very strong. They also showed that the produced turbulence is advected into the coherent vortex, where most of the turbulence dissipation occurs. Their findings can be used to interpret our observations. In figure 8, the separated shear layer behind the ripple crest is quite significant within about ±40° from the phase of maximum free-stream velocity (i.e., $\theta = 0°$), so a substantial amount of turbulence is produced and subsequently fed into the growing lee vortex, leading to the increase of turbulence intensity. From $\theta = 45°$ onward, the free-stream flow has been reduced a lot, so the flow separation and hence the shear production of turbulence behind the ripple crest are dramatically reduced. The coherent vortex cannot receive enough 'feeding' of turbulence, so the embedded turbulence decays in the remaining of vortex's life cycle ($\theta = 45°$ to $160°$) due to local dissipation. The ejected coherent vortex can carry some residual turbulence to the other side of ripple crest (e.g. figure 8 f-h), but the intensity of residual turbulence seems to be very low. The residual turbulence more-or-less dies out when the next coherent vortex begins its life cycle (e.g. figure 8i).

The measurements suggest that we can take the coherent vortex as a proxy of flow turbulence, since their life journeys are fairly synchronized. We have shown that acceleration skewness differentiates the two coherent vortices of a wave cycle (as shown in section 3), so there must also be some effects on the temporal-spatial variations of turbulence, which will be presented in the next subsection.

4.2. The effect of acceleration skewness on turbulence

The discussions on the effect of acceleration skewness on turbulence are based on two tests, TA060b and TA060a, in this study. figures 9 and 10 show the snapshots of turbulence intensity over a whole flow cycle for these two tests, respectively. Here we we separate each half-cycle into an accelerating quarter (u_∞ from 0 to maximum) and a decelerating quarter (u_∞ from maximum to 0), and three snapshots are presented for each quarter.

In both figures 9 and 10, b-d shows the onshore decelerating quarter, e-g shows the offshore accelerating quarter, h-j shows the offshore decelerating quarter, and k-m shows the onshore accelerating quarters.

We start with some discussions for the low acceleration-skewed test, Ta060b, and the focus here is on how acceleration skewness differentiates the two half cycles and the two coherent vortices. We first consider the decelerating quarters, in which the coherent vortex and the associated flow turbulence reach their maximum intensity (as revealed by the sinusoidal-flow test in section 4.1). Comparing figure 9 b-d with h-j, it can be clearly seen that the offshore vortex (in h-j) has much higher turbulence intensity than the onshore vortex. The difference is already significant at the beginning of the decelerating quarter, i.e., the turbulence within offshore vortex in figure 9h is much stronger than the turbulence within the onshore vortex in figure 9b. Note that the coherent vortex and the associated turbulence begin to develop within the later stage of an accelerating quarter. acceleration skewness elongates the duration of the offshore accelerating quarter but reduces the duration of the onshore accelerating quarter. Therefore, the offshore vortex has more time to develop its turbulence than the onshore vortex within their corresponding accelerating quarters. This possibly explains why the offshore vortex is more turbulent than the onshore vortex at the beginning of the decelerating quarter. In other words, acceleration skewness gives the offshore vortex a ‘head start’ for developing its turbulence in the decelerating quarter. This ‘head start’ leads to the difference between figure 9 b-d and h-j. We now consider the accelerating quarters, in which the key flow feature is the ejection of the coherent vortex developed from the preceding half-cycle. Comparing figure 9 k with e, we can see that the offshore vortex is more turbulent than the offshore vortex at the moment of flow reversal ($u_\infty = 0$). Subsequently, it seems that the offshore vortex can carry slightly more residual turbulence over the ripple crest than the onshore vortex does (figure 9 l-m vs. f-g). The intensity of the residual turbulence remains very low, as in the sinusoidal-flow test (SIN60).

The difference between the two accelerating quarters are much more pronounced for test ASY60a shown in figure 10. The offshore accelerating quarter of this test is similar to that of test ASY60b (i.e., figure 10 e-g are similar to figure 9 e-g), but the onshore accelerating quarter (figure 10 k-m), instead of being ‘quite’, has a very strong overall turbulence intensity, which is mainly because of the strong residual turbulence carried by the offshore vortex. As discussed in section 3, acceleration skewness reduces the residence time of the offshore vortex within its born site. In addition, the increased flow acceleration within the onshore accelerating quarter gives a faster ambient flow for moving the ejected offshore vortex to the ripple crest. As a result, the residual turbulence in the offshore vortex has less time to dissipate, so a significant amount of residual turbulence can reach the ripple crest, as shown in figure 10i. The shear production of turbulence kinematic energy, $P_{tke} = -\widetilde{u_i' u_j'} S_{ij}$, is determined by the Reynolds stress tensor $-\widetilde{u_i' u_j'}$ and the rate of strain S_{ij}. Here we can take the turbulence intensity as a surrogate of $-\widetilde{u_i' u_j'}$. When a substantial amount of residual turbulence carried by the offshore vortex reaches the ripple crest and subsequently the onshore-side ripple flank, it interacts with the high local rate of strain near the ripple surface, so the local shear production is significantly enhanced. This explains why high turbulence intensity occurs near the ripple crest in figure 10 i and m, which is not seen in figure 9 i and m or figure 10 f and g. In other words, the residual turbulence provided by the offshore vortex gives the next onshore vortex a ‘head start’ for developing its turbulence. As a result, the turbulence intensity of the onshore vortex is greatly enhanced within the onshore decelerating quarter. We can see that the turbulence intensity in the three snapshots of the onshore decelerating quarter (figure 10 b-d) is comparable to that in the three snapshots of the offshore decelerating quarter (figure 10 h-j), which is not true for TA060b in figure 9. Since the onshore decelerating quarter is elongated by acceleration skewness, there is more time for dissipating the turbulence within the onshore vortex before the flow reversal. As a result, there is still little residual turbulence of the onshore vortex passes the ripple crest (see figure 10f).

In summary, the acceleration skewness enhances the flow turbulence within the offshore vortex, and allows more residual turbulence in the offshore vortex to move across the ripple crest. For the onshore vortex, the flow turbulence can be either increased (as in TA060a) or decreases (as in TA060b) by acceleration skewness, but the amount of residual turbulence crossing the ripple crest always remains low.

5. Form drag

The presence of coherent vortex alters the pressure distribution around the vortex ripple and therefore leads to a net streamwise pressure force, which is often referred to as the form drag. Here we investigate this phenomenon based on our flow measurements. For 2-dimensional flow, the governing equation for the vertical component of phase-averaged velocity, w, i.e.,

$$\frac{\partial w}{\partial t}+\frac{\partial uw}{\partial x}+\frac{\partial ww}{\partial z}=-\frac{1}{\rho}\frac{\partial p}{\partial z}-\frac{\partial \widetilde{u'w'}}{\partial x}-\frac{\partial \widetilde{w'w'}}{\partial z} \tag{10}$$

is integrated from the free-stream to a specific level z, which gives

$$\frac{p'}{\rho}=\int_z^\infty \frac{\partial w}{\partial t}dz+\int_z^\infty \frac{\partial uw}{\partial x}dz-ww+\int_z^\infty \frac{\partial \widetilde{u'w'}}{\partial x}dz-\widetilde{w'w'} \tag{11}$$

where $p' = p - p_\infty$. Here we assumed $ww = 0$ and $\widetilde{w'w'} = 0$ at $z = \infty$. Note that p' is the change of water pressure from the free-stream value, which is the source of form drag. Thus, we obtained the form drag by integrating $p'(x, z_b)dz_b/dx$ over a ripple length, where z_b denotes the ripple surface. To compare form drag with flat-bed bottom shear stress, the result is normalized as

$$f = \frac{2}{\rho {U_{\infty,1}}^2 \lambda} \int_\lambda p'(x, z_b) \frac{dz_b}{dx} dx \qquad (12)$$

Note that f ~O(0.001~0.01) for a flat rough bed with a small bottom roughness ($A_b/k_b \gg 1$, where A_b is the excursion amplitude and k_b is bottom roughness).

Figure 11 presents the normalized $p^* = p'/(\rho U_{\infty,1}^2)$ for test ASY60a. Overall speaking, the coherent vortices produce negative p^* locally, and carry the region of negative p^* with them. At the phases of peak values of u_∞ (see figure 11 b and h), very strong negative p^* is located within the growing lee vortex, which covers a region fairly close to the ripple surface. As u_∞ decelerates, the negative p^* zone follows the lee vortex to move slightly away from the ripple crest. During this process the negative p^* zone expands in area but decreases in magnitude. When a lee vortex is washed over the ripple crest, the negative p^* within it becomes secondary compared to the negative p^* within the newborn lee vortex (see figure 11 f and i). As a lee vortex moves away from its born site, positive p^* starts to fill in the region that is previously occupied by the lee vortex, e.g., positive p^* is found underneath the dislodged offshore vortex at the phase when $u_\infty = 0$ (figure 11 k). As the u_∞ accelerates (e.g. figure 11 l and m), the zone of positive p^* is extended to most of the stoss side and part of the lee side. The magnitude of positive p^* also increases as u_∞ accelerates.

Figure 12 presents the normalized form drag, f, together with the free-stream velocity for the four tests involved in this study. It can be seen that the peak magnitudes, f_{max}, is about 0.1∼0.15 for these tests, and the temporal variation of f is similar to that of u_{∞}, but f seems to lead u_{∞} with a phase lead (about 10∼30°), and there are multiple peaks in the time series of f within a half cycle. Test SIN60 was also covered in a previous study of *Yuan and Wang* [2018], in which the total resistance for sinusoidal flows over vortex ripples was estimated from measurements of water pressure. In their study, f_{max} was about 0.18 for test SIN60, which is a bit larger than f_{max}=0.12 in this study, but the temporal variation of f is quite similar to that shown in figure 12d. The difference in f_{max} is possibly due to the skin shear stress, which is included in the total flow resistance. In the earlier studies by *Carstens et al.* [1969] and *Lofquist* [1986], the f_{max} values can be even larger (0.2 to 0.4), which is possibly because of the relatively smaller scale of their tests [discussed by *Yuan and Wang*, 2018]. The snapshots of p^* allows us to interpret the key features of f. For all tests, a primary peak of f in each half-cycle occurs around or slightly after the phase of peak u_{∞}. As shown in figure 11 b and h, at these moments the lee side is covered by a negative p^* zone produced by the growing lee vortex, while the stoss side is covered by a positive p^* zone, so a positive streamwise pressure force is produced. Note that the magnitude of negative p^* within the lee vortex is strongest around the phase of peak u_{∞}, so a local peak of form drag is produced. A secondary peak of f occurs about 60-80° before the primary peak, e.g., around $\theta = -70°$ or 290° in figure 12a. These moments are within the early stage of accelerating quarters, and the ejected vortex from the previous half-cycle is about to pass the ripple crest. As shown in figure 11 k-m, the distributions of positive and negative p^* on the ripple surface change as the ejected lee vortex passes the ripple crest. When the ejected vortex reaches the ripple crest, the pressure distribution is similar to that at the phase of peak u_∞ (figure 11b), i.e., positive p^* over the stoss side and negative p^* over the lee side, so a large form drag is produced. Slightly after this phase, the pressure distribution is rather symmetric regarding the ripple crest (e.g., figure 11m), leading to a reduction of net pressure force or form drag. This explains the secondary peak of f.

The effect of acceleration skewness on form drag is mainly making the temporal variation of form drag follow that of free-stream velocity. There is little difference in the maximum form drag between the two half-cycles. The data suggests that the dominant contributors to p^* in equation (11) are the two terms involving the phase-averaged flow. As can be seen by comparing figure 11 b and h, the two phases of peak onshore and offshore u_∞ are quite similar in terms of the phase-averaged velocity, so they have similar instantaneous p^* distribution and form drag.

6. Conclusion

A full-scale experimental study on acceleration-skewed oscillatory flows over vortex ripples has been conducted using an oscillatory water tunnel, which produces bottom-parallel oscillatory flows as approximations of wave-driven near-bed flows. Three acceleration-skewed-flow tests and a sinusoidal-flow test were involved in this study. 2-dimensional vortex ripples were generated from a coarse-sand movable bed. A 2-dimensional PIV system was deployed to measure the flow field around a whole ripple. The PIV measurements were separated into phase-averaged flows and turbulent fluctuations for further analysis.

In each half-cycle, a coherent vortex starts to grow as the free-stream flow accelerates towards the peak value, and reaches its maximum strength shortly after the phase of peak free-stream velocity. As the free-stream flow further decelerates, the lee vortex moves towards the ripple crest, while its strength decays. It is eventually washed over the ripple crest slightly after the flow reversal, and subsequently drifts with the ambient flow until vanished. The main effect of acceleration skewness on vortex dynamics is that it decreases the residence time of the offshore vortex by expediting the offshore-onshore flow reversal, while the opposite occurs for the onshore vortex. Among our acceleration-skewed-flow tests, the residence time of the offshore vortex can be 50% shorter than that of the onshore vortex.

The phase-averaged flow is ripple-averaged to investigate whether an analogy can be drawn between the acceleration-skewed oscillatory flows over flat beds and rippled beds. The primary two harmonics of streamwise velocity have similar features as those in flat-bed scenarios. The amplitude profiles have an overshoot structure slightly above the ripple crest. The near-bed flow leads the free-stream flow by up to 40-50° in phase. The snapshots of phase-averaged flow fields show that the features of ripple-averaged flow can be well explained by the generation-ejection process of coherent vortices. For acceleration-skewed-flow tests, the instantaneous boundary layer thickness at the phase of peak onshore free-stream velocity is thinner than that at the phase of peak offshore free-stream velocity, which follows the general argument that describes how acceleration skewness affects boundary layer thickness for flat-bed scenarios. The cycle- and ripple-averaged streamwise velocity is negative near the ripple and positive at higher levels, which also agrees with what has been observed in flat-bed OWT studies. Therefore, our measurements generally suggest a possibility that the ripple-averaged flow can be conceptualized as a flat-bed flow when modelling the effect of acceleration skewness.

As observed in previous studies, turbulence is mainly distributed within the coherent vortices. The effect of acceleration skewness on the turbulence of the two coherent vortices are as follows. For the offshore vortex, acceleration skewness enhances the development of turbulence within the offshore vortex by elongating the offshore accelerating quarter. In addition, acceleration skewness expedites the ejection process of the offshore vortex, allowing more residual turbulence of the offshore vortex to cross the ripple crest. The effect of acceleration skewness on onshore vortex is twofold. Firstly, it shortens the onshore accelerating quarter, which suppresses the development of turbulence. This effect is pronounced if the acceleration skewness is low. Secondly, the increased amount of residual turbulence from offshore vortex boosts the production of turbulence within the onshore vortex, which can be the dominant effect if the acceleration skewness is high. The residual turbulence of the onshore vortex reaching the offshore side is always low, regardless of how acceleration skewness affects the turbulence of the onshore vortex.

The ripple-induced pressure, p', which is the difference between local and free-stream pressure, is determined by vertically integrating the governing equation for vertical phase-averaged velocity component. The form drag, which is the normalized streamwise pressure force, is obtained from the p' field. Two peaks of form drag within each half-cycle are observed for all tests. The first peak is around or slightly after the phase of peak free-stream velocity, and the second peak is around the phase when a ejected vortex passes the ripple crest. The magnitude of maximum form drag agrees with some previous observations, and it is also observed that the form drag leads the free-stream velocity in phase (by roughly $10 \sim 30^\circ$). acceleration skewness does not lead to a noticeable difference between the maximums of onshore and offshore form drag.

A key effect of acceleration skewness on the turbulence intensity is that the offshore vortex can carry more residual turbulence across the ripple crest than the onshore vortex. If we use turbulence as a proxy of sediment suspension, an immediate implication is that the offshore vortex can carry more sand grains across the ripple crest than the onshore vortex. Therefore, an onshore net (cycle-averaged) sediment transport rate should be expected. To confirm this, the net sediment transport rate was measured for two tests, ASY60a and ASY45a, based on the conservation of sand volume and the measurements of bottom profile [details of the methodology are presented in *Wang and Yuan*, 2018]. For both tests, the net transport rates are indeed onshore, and the magnitudes are $8.1 \cdot 10^{-6}$ m^2/s (ASY45a) and $20.6 \cdot 10^{-6}$ m^2/s (ASY60a). Note that velocity-skewed oscillatory flows over vortex ripples will produce an offshore net sediment transport rate [e.g. *Nielsen et al.*, 1978; *Sato*, 1986; *van der Werf et al.*, 2007], of which the magnitude is also of $\mathrm{O}(10^{-6} \sim 10^{-5}\ \mathrm{m}^2/\mathrm{s})$. This is because the onshore vortex is significantly stronger than the offshore vortex under velocity-skewed flows. Thus, acceleration skewness and velocity skewness have opposite contributions to net sediment transport rate, which must be adequately accounted for in modelling wave-driven net sediment transport rate over rippled beds.

This paper focuses on the coherent vortex, which plays a dominant role in determining the suspended-load sediment transport over a vortex ripple. The sediment movement within a few sediment diameters from the rippled bed can also contribute to the total sediment transport. To understand the near-bed sediment transport, it is desirable to have some in-depth knowledge on the bottom shear stress and the near-bed flow velocity. Unfortunately, our tests cannot provide very reliable measurements in the immediate vicinity of the ripple surface. This is partly because the no-motion sand bed keeps deforming within a flow cycle, and it is sometimes impossible to track the ripple surface from a single PIV image. Also, the high local sediment concentration makes the local PIV measurements questionable. In the future, perhaps other flow measurement methods, such as some acoustic or conductivity profilers [e.g. *Fromant et al.*, 2018], can be applied for obtaining reliable near-bed measurements.

Acknowledgments. The authors gratefully acknowledge the financial support from the Tier-1 research project funded by the Ministry Of Education of Singapore (WBS: R-302-000-126-112). Data presented in this paper can be accessed through the ScholarBank repository of National University of Singapore: https://doi.org/10.25540/EJ2Z-9001.

References

Ayrton, H. (1910), The origin and growth of ripple-mark, *Proceedings of the Royal Society of London. Series A, Containing Papers of a Mathematical and Physical Character*, *84*(571), 285–310, doi:doi:10.1098/rspa.1910.0076.

Bagnold, R. A. (1946), Motion of waves in shallow water. interaction between waves and sand bottoms, *Proceedings of the Royal Society of London. Series A, Mathematical and Physical Sciences*, pp. 1–18.

Blondeaux, P. (1990), Sand ripples under sea waves part 1. ripple formation, *Journal of Fluid Mechanics*, *218*, 1–17, doi:10.1017/S0022112090000908.

Blondeaux, P., and G. Vittori (1991), Vorticity dynamics in an oscillatory flow over a rippled bed, *Journal of Fluid Mechanics*, *226*, 257–289, doi:10.1017/S0022112091002380.

Blondeaux, P., P. Scandura, and G. Vittori (2004), Coherent structures in an oscillatory separated flow: numerical experiments, *Journal of Fluid Mechanics*, *518*, 215–229, doi:

doi:10.1017/S0022112004000953.

Carstens, M., F. Neilson, and H. Altinbilek (1969), *Bed Forms Generated in the Laboratory Under an Oscillatory Flow: Analytical and Experimental Study, Tech. Memo. 28*, U.S. Army Corps of Engineers, Coastal Engineering Research Center.

Chakraborty, P., S. Balachandar, and R. J. Adrian (2005), On the relationships between local vortex identification schemes, *Journal of Fluid Mechanics*, *535*, 189–214, doi:10.1017/S0022112005004726.

Darwin, G. H. (1883), I. on the formation of ripple-mark in sand, *Proceedings of the Royal Society of London*, *36*(228-231), 18–43, doi:doi:10.1098/rspl.1883.0077.

Earnshaw, C. H., and A. C. Greated (1998), Dynamics of ripple bed vortices, *Experiments in Fluids*, *25*(3), 265–275, doi:10.1007/s003480050229.

Einstein, H. A., and N. Chien (1955), *Effects of heavy sediment concentration near the bed on velocity and sediment distribution*, , technical report, Inst. of Eng. Res. Univ. of Calif., Berkeley.

Elfrink, B., D. M. Hanes, and B. G. Ruessink (2006), Parameterization and simulation of near bed orbital velocities under irregular waves in shallow water, *Coastal Engineering*, *53*(11), 915–927, doi:http://dx.doi.org/10.1016/j.coastaleng.2006.06.002.

Fredsøe, J., K. H. Andersen, and B. Mutlu Sumer (1999), Wave plus current over a ripple-covered bed, *Coastal Engineering*, *38*(4), 177–221, doi:10.1016/s0378-3839(99)00047-2.

Fromant, G., R. S. Mieras, T. Revil-Baudard, J. A. Puleo, D. Hurther, and J. Chauchat (2018), On bedload and suspended load measurement performances in sheet flows using acoustic and conductivity profilers, *Journal of Geophysical Research: Earth Surface*, *123*(10), 2546–2562, doi:10.1029/2017jf004560.

Giménez-Curto, L. A., and M. A. C. Lera (1996), Oscillating turbulent flow over very rough surfaces, *Journal of Geophysical Research: Oceans*, *101*(C9), 20,745–20,758, doi: doi:10.1029/96JC01824.

Grigoriadis, D. G. E., A. A. Dimas, and E. Balaras (2012), Large-eddy simulation of wave turbulent boundary layer over rippled bed, *Coastal Engineering*, *60*, 174–189, doi:10.1016/j.coastaleng.2011.10.003.

Hare, J., A. E. Hay, L. Zedel, and R. Cheel (2014), Observations of the space-time structure of flow, turbulence, and stress over orbital-scale ripples, *Journal of Geophysical Research: Oceans*, *119*(3), 1876–1898, doi:10.1002/2013JC009370.

Herrmann, M., and O. S. Madsen (2007), Effect of stratification due to suspended sand on velocity and concentration distribution in unidirectional flows, *Journal of Geophysical Research*, *112*(C02006).

Hurther, D., and P. D. Thorne (2011), Suspension and near-bed load sediment transport processes above a migrating, sand-rippled bed under shoaling waves, *Journal of Geophysical Research: Oceans*, *116*, C07,001, doi:10.1029/2010JC006774.

Jiménez, J. A., and O. S. Madsen (2003), A simple formula to estimate settling velocity of natural sediments, *Journal of Waterway, Port, Coastal, and Ocean Engineering*, *129*(2), 70–78, doi:doi:10.1061/(ASCE)0733-950X(2003)129:2(70).

Lofquist, K. E. B. (1986), *Drag on naturally rippled beds under oscillatory flows*, Miscellaneous paper ;CERC-86-13, U.S. Army Engineer Waterways Experiment Station, Vicksburg, Mississippi.

Longuet-Higgins, M. S. (1953), Mass transport in water waves, *Philosophical Transactions of the Royal Society of London. Series A, Mathematical and Physical Sciences*, *245*(903), 535–581.

Longuet-Higgins, M. S. (1981), Oscillating flow over steep sand ripples, *Journal of Fluid Mechanics*, *107*, 1–35.

Malarkey, J., and A. G. Davies (2002), Discrete vortex modelling of oscillatory flow over ripples, *Applied Ocean Research*, *24*(3), 127–145, doi:http://dx.doi.org/10.1016/S0141-1187(02)00035-4.

Mathisen, P. P. (1989), Experimental study on the response of fine sediments to wave agitation and associated wave attenuation, Master's thesis, Massachusetts Institute of Technology, Cambridge, MA, U.S.

Maxey, M. R., and S. Corrsin (1986), Gravitational settling of aerosol particles in randomly oriented cellular flow fields, *Journal of the Atmospheric Sciences*, *43*(11), 1112–1134, doi:10.1175/1520-0469(1986)043¡1112:Gsoapi¿2.0.Co;2.

Nakato, T., J. F. Kennedy, J. R. Glover, and F. A. Locher (1977), Wave entrainment of sediment from rippled beds, *Journal of the Waterway, Port, Coastal and Ocean Division*, *103*, 83–99.

Nichols, C., and D. Foster (2007), Full-scale observations of wave-induced vortex generation over a rippled bed, *Journal of Geophysical Research: Oceans*, *112*(C10).

Nielsen, P. (1983), Analytical determination of nearshore wave height variation due to refraction shoaling and friction, *Coastal Engineering*, *7*(3), 233–251.

Nielsen, P. (1992), *Coastal Bottom Boundary Layers and Sediment Transport*, World Scientific Publishing.

Nielsen, P. (2009), *Coastal and Estuarine Processes*, World Scientific Publishing.

Nielsen, P. (2016), 1dv structure of turbulent wave boundary layers, *Coastal Engineering*, *112*, 1–8, doi:https://doi.org/10.1016/j.coastaleng.2016.02.001.

Nielsen, P., I. Svensen, and C. Staub (1978), Onshore-offshore sediment movement on a beach, in *Proceedings of the 16th International Conference on Coastal Engineering*, pp. 1475–1492.

O'Donoghue, T., and S. Wright (2004), Flow tunnel measurements of velocities and sand flux in oscillatory sheet flow for well-sorted and graded sands, *Coastal Engineering*, *51*(11–12), 1163–1184, doi:10.1016/j.coastaleng.2004.08.001.

O'Donoghue, T., J. S. Doucette, J. J. van der Werf, and J. S. Ribberink (2006), The dimensions of sand ripples in full-scale oscillatory flows, *Coastal Engineering*, *53*(12), 997–1012, doi:http://dx.doi.org/10.1016/j.coastaleng.2006.06.008.

Pedocchi, F., and M. H. García (2009), Ripple morphology under oscillatory flow: 1. prediction, *Journal of Geophysical Research: Oceans*, *114*(C12), C12,014, doi:10.1029/2009JC005354.

Pope, S. (2000), *Turbulent Flows*, Cambridge University Press.

Rankin, K. L., and R. I. Hires (2000), Laboratory measurement of bottom shear stress on a movable bed, *Journal of Geophysical Research: Oceans*, *105*(C7), 17,011–17,019, doi:10.1029/2000JC900059.

Ribberink, J. S., and A. A. Al-Salem (1995), Sheet flow and suspension of sand in oscillatory boundary layers, *Coastal Engineering*, *25*(3-4), 205–225.

Rodríguez-Abudo, S., and D. L. Foster (2014), Unsteady stress partitioning and momentum transfer in the wave bottom boundary layer over movable rippled beds, *Journal of Geophysical Research: Oceans*, *119*(12), 8530–8551, doi:10.1002/2014JC010240.

Sand Jespersen, T., J. Q. Thomassen, A. Andersen, and T. Bohr (2004), Vortex dynamics around a solid ripple in an oscillatory flow, *Eur. Phys. J. B*, *38*(1), 127–138.

Sato, S. (1986), Oscillatory boundary layer flow and sand movement over ripples, Ph.D. thesis, University of Tokyo.

Sato, S., and K. Horikawa (1986), Laboratory study on sand transport over ripples due to asymmetric oscillatory flows, in *Proceedings of the 20th International Conference on Coastal Engineering*, pp. 1481–1495.

Sato, S., N. Mimura, and A. Watanabe (1984), Oscillatory boundary layer flow over rippled beds, in *Proceedings of the 19th International Conference on Coastal Engineering*, pp. 2293–2309, ASCE.

Sato, S., H. Uehara, and A. Watanabe (1986), Numerical simulation of the oscillatory boundary layer flow over ripples by a $k-\epsilon$ turbulence model, *Coastal Engineering in Japan*, *29*(1), 65–78, doi:10.1080/05785634.1986.11924428.

Sato, S., K.-i. Shimosako, and A. Watanabe (1987), Measurements of oscillatory turbulent boundary layer flow above ripples with a laser-doppler velocimeter, *Coastal Engineering in Japan*, *30*(1), 89–98, doi:10.1080/05785634.1987.11924466.

Scandura, P., G. Vittori, and P. Blondeaux (2000), Three-dimensional oscillatory flow over steep ripples, *Journal of Fluid Mechanics*, *412*, 355–378, doi: doi:10.1017/S0022112000008430.

Sleath, J. F. A. (1982), Friction coefficients of rippled beds in oscillatory flow, *Continental Shelf Research*, *1*(1), 33–47, doi:https://doi.org/10.1016/0278-4343(82)90031-0.

Snyder, W. H., and J. L. Lumley (1971), Some measurements of particle velocity autocorrelation functions in a turbulent flow, *Journal of Fluid Mechanics*, *48*(1), 41–71, doi:10.1017/S0022112071001460.

Styles, R., and S. M. Glenn (2000), Modeling stratified wave and current bottom boundary layers on the continental shelf, *Journal of Geophysical Research: Oceans*, *105*(C10), 24,119–24,139, doi:10.1029/2000JC900115.

Toit, C. G. D., and J. F. A. Sleath (1981), Velocity measurements close to rippled beds in oscillatory flow, *Journal of Fluid Mechanics*, *112*, 71–96, doi: 10.1017/S002211208100030X.

Tunstall, E. B., and D. L. Inman (1975), Vortex generation by oscillatory flow over rippled surfaces, *Journal of Geophysical Research*, *80*(24), 3475–3484, doi: doi:10.1029/JC080i024p03475.

van der A, D. A., T. O'Donoghue, and J. S. Ribberink (2010), Measurements of sheet flow transport in acceleration-skewed oscillatory flow and comparison with practical formulations, *Coastal Engineering*, *57*(3), 331–342.

van der A, D. A., T. O'Donoghue, A. G. Davies, and J. S. Ribberink (2011), Experimental study of the turbulent boundary layer in acceleration-skewed oscillatory flow, *Journal of Fluid Mechanics*, *684*, 251–283.

van der Werf, J. J., J. S. Ribberink, T. O'Donoghue, and J. S. Doucette (2006), Modelling and measurement of sand transport processes over full-scale ripples in oscillatory flow, *Coastal Engineering*, *53*(8), 657–673, doi: http://dx.doi.org/10.1016/j.coastaleng.2006.02.002.

van der Werf, J. J., J. S. Doucette, T. O'Donoghue, and J. S. Ribberink (2007), Detailed measurements of velocities and suspended sand concentrations over full-scale ripples in regular oscillatory flow, *Journal of Geophysical Research: Earth Surface*, *112*(F2), F02,012, doi:10.1029/2006JF000614.

van der Werf, J. J., V. Magar, J. Malarkey, K. Guizien, and T. O'Donoghue (2008), 2dv modelling of sediment transport processes over full-scale ripples in regular asymmetric oscillatory flow, *Continental Shelf Research*, *28*(8), 1040–1056, doi: http://dx.doi.org/10.1016/j.csr.2008.02.007.

Wang, D., and J. Yuan (2018), Bottom-slope-induced net sediment transport rate under oscillatory flows in the rippled-bed regime, *Journal of Geophysical Research: Oceans*, *123*(10), 7308–7331, doi:doi:10.1029/2018JC013810.

Wiberg, P. L., and C. K. Harris (1994), Ripple geometry in wave-dominated environments, *Journal of Geophysical Research: Oceans*, *99*(C1), 775–789, doi:10.1029/93JC02726.

Yuan, J., and O. S. Madsen (2014), Experimental study of turbulent oscillatory boundary layers in an oscillating water tunnel, *Coastal Engineering*, *89*, 63–84, doi: http://dx.doi.org/10.1016/j.coastaleng.2014.03.007.

Yuan, J., and O. S. Madsen (2015), Experimental and theoretical study of wave–current turbulent boundary layers, *Journal of Fluid Mechanics*, *765*, 480–523.

Yuan, J., and D. Wang (2018), Experimental investigation of total bottom shear stress for oscillatory flows over sand ripples, *Journal of Geophysical Research: Oceans*, *123*(9), 6481–6502, doi:doi:10.1029/2018JC013953.

Yuan, J., Z. Li, and O. S. Madsen (2017), Bottom-slope-induced net sheet-flow sediment transport rate under sinusoidal oscillatory flows, *Journal of Geophysical Research: Oceans*, *122*(1), 236–263, doi:10.1002/2016JC011996.

Zedler, E. A., and R. L. Street (2006), Sediment transport over ripples in oscillatory flow, *Journal of Hydraulic Engineering*, *132*(2), 180–193, doi:doi:10.1061/(ASCE)0733-

9429(2006)132:2(180).

Zhou, J., R. J. Adrian, S. Balachandar, and T. Kendall (1999), Mechanisms for generating coherent packets of hairpin vortices in channel flow, *Journal of fluid mechanics*, *387*, 353–396.

Önder, A., and J. Yuan (2019), Turbulent dynamics of sinusoidal oscillatory flow over a wavy bottom, *Journal of Fluid Mechanics*, *858*, 264–314, doi:10.1017/jfm.2018.754.

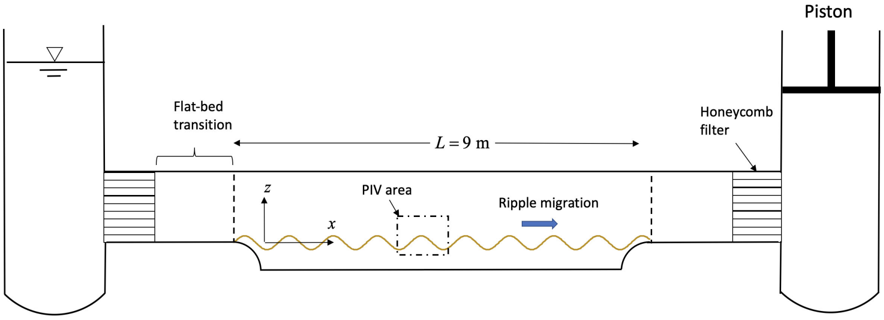

Figure 1. Sketch of the WCS facility

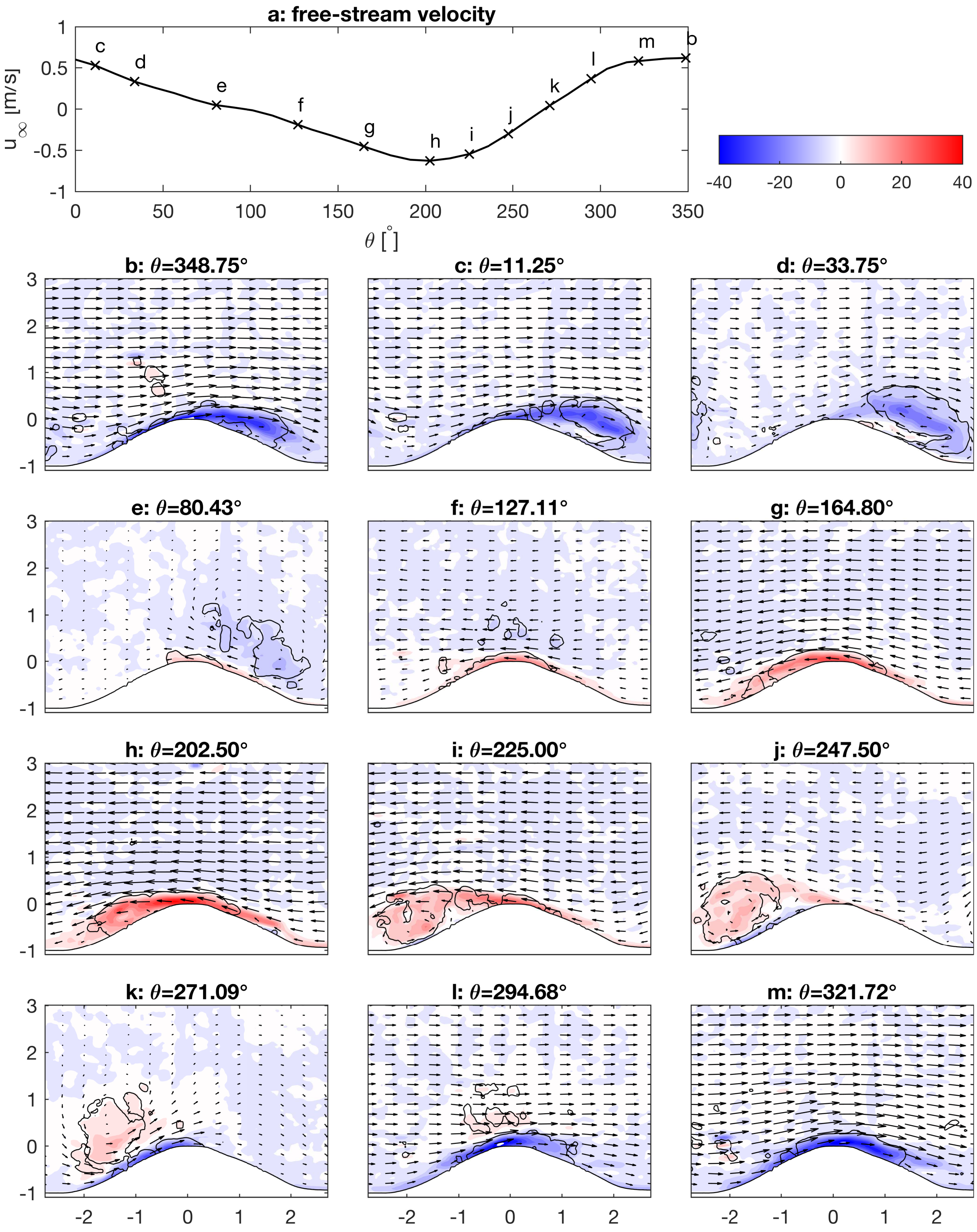

Figure 2. Vorticity of the phase-averaged flow velocity of test ASY60a (the x and z coordinates in figure b-m are normalized by ripple height, i.e., $x^* = x/\eta$ and $z^* = z/\eta$, and the solid contours indicate Λ_i^*=1).

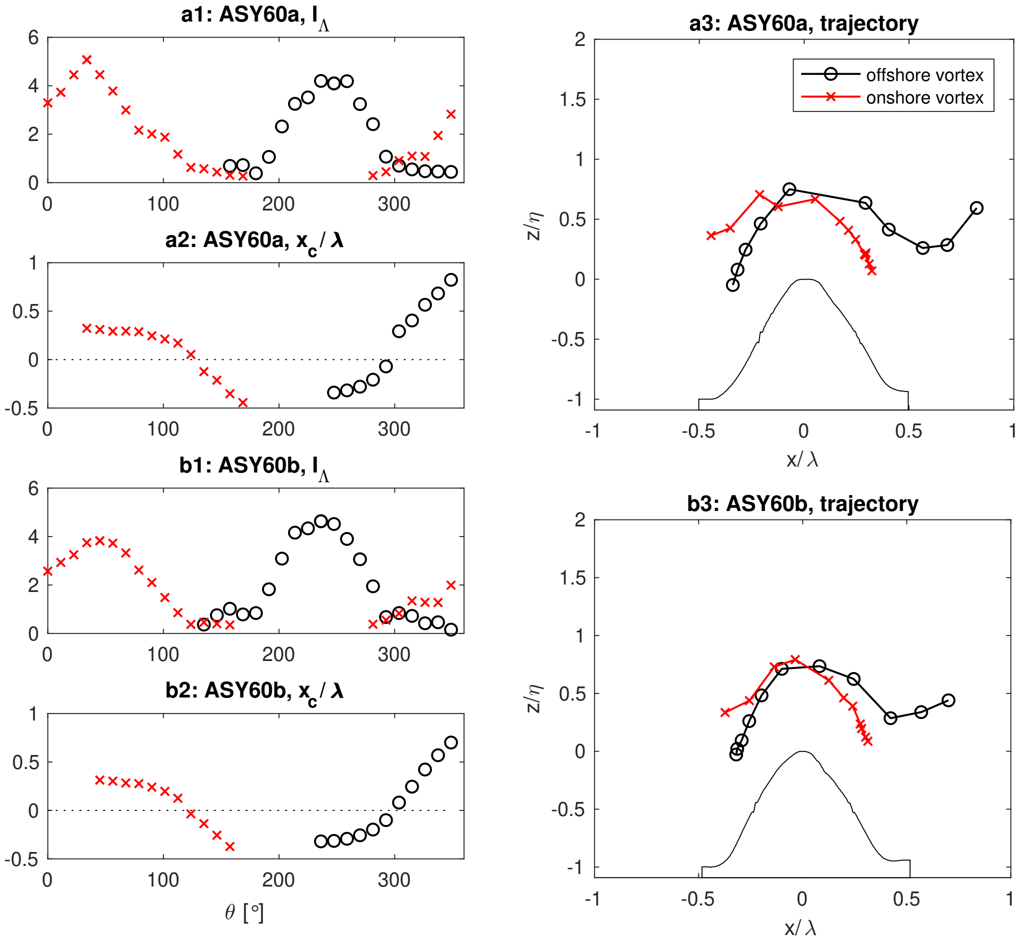

Figure 3. Trajectories of ejected coherent vortices and the integrated swirling length.

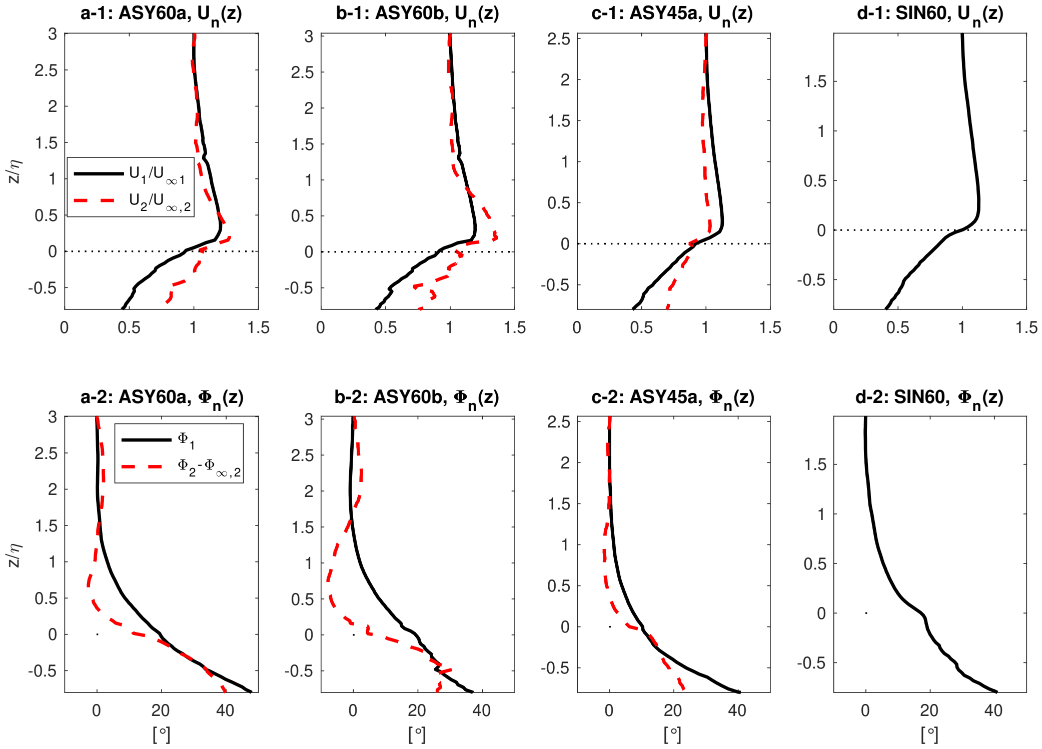

Figure 4. First and second harmonics of ripple- and phase-averaged streamwise velocity.

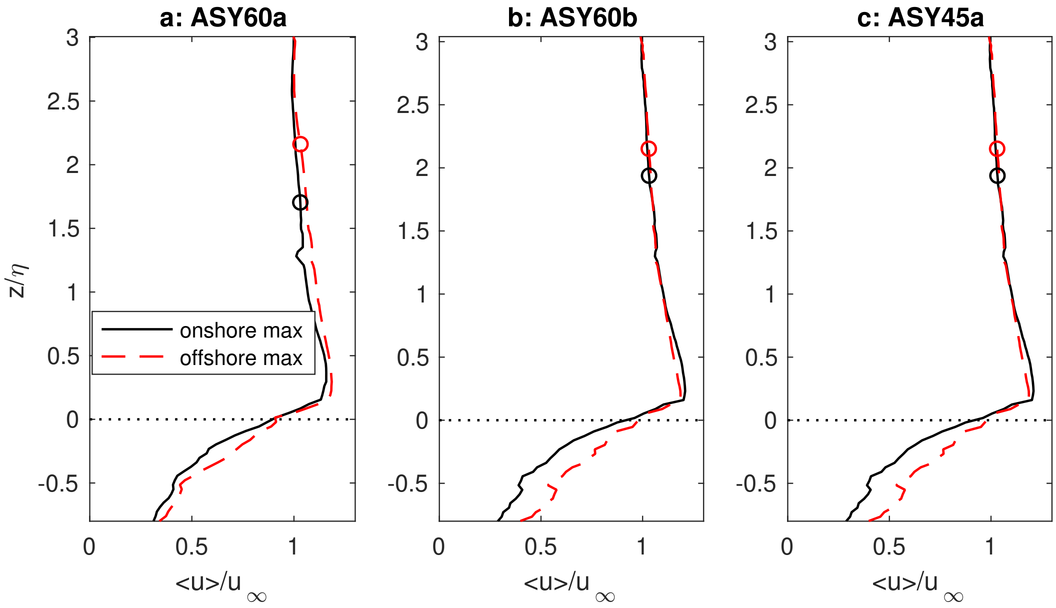

Figure 5. Profiles of ripple- and phase-averaged streamwise velocity at the phases of peak onshore and offshore free-stream velocity (the circles indicate the location where local velocity deviates from the free-stream value by 3%).

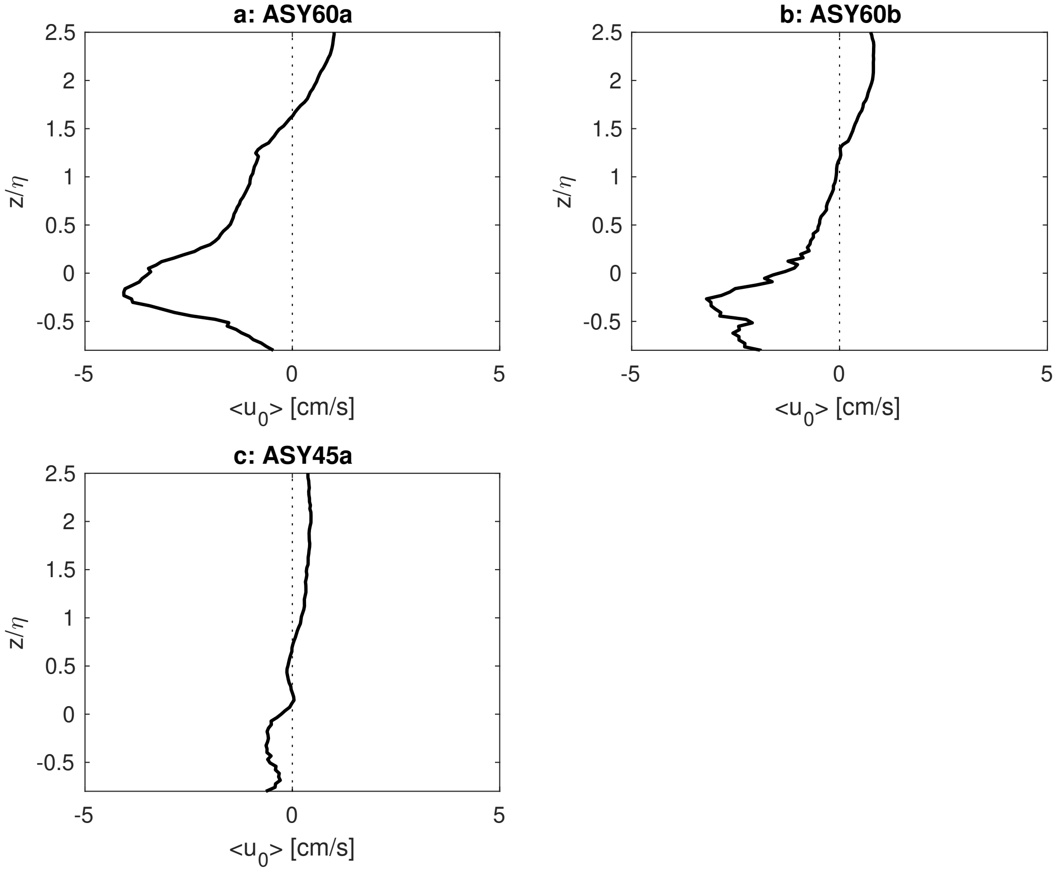

Figure 6. Cycle- and ripple-averaged streamwise velocity profiles for the three acceleration-skewed-flow tests.

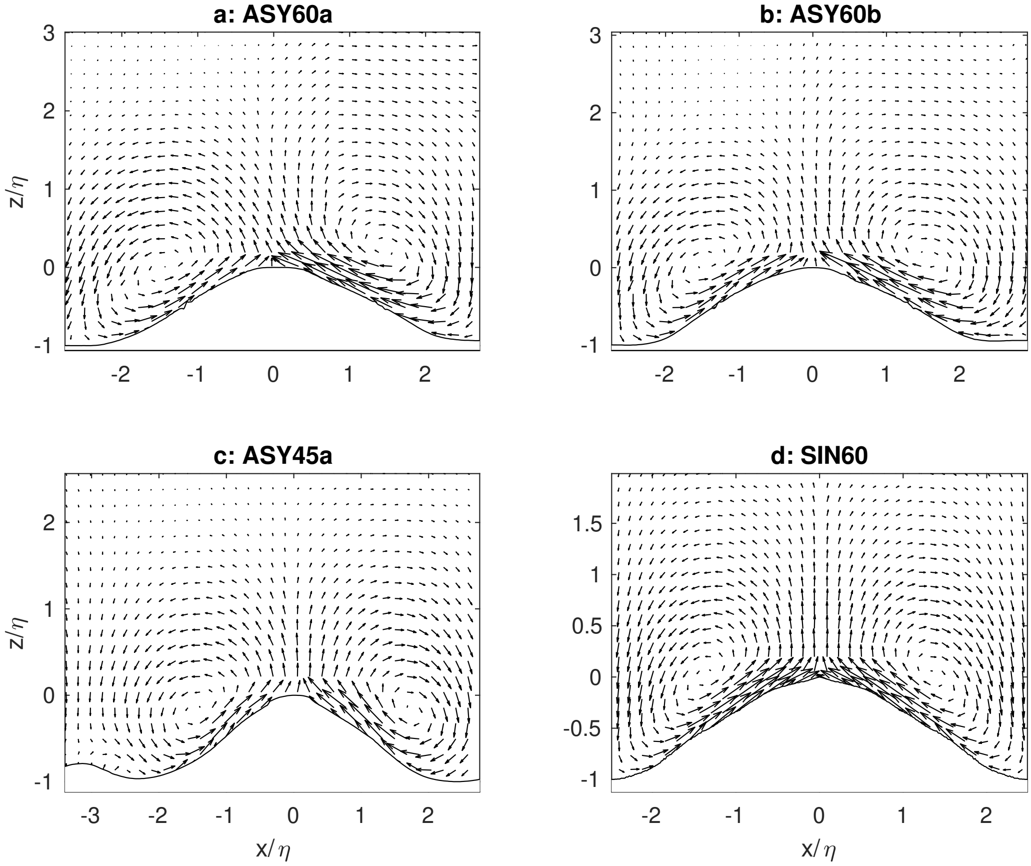

Figure 7. Cycle-averaged velocity fields

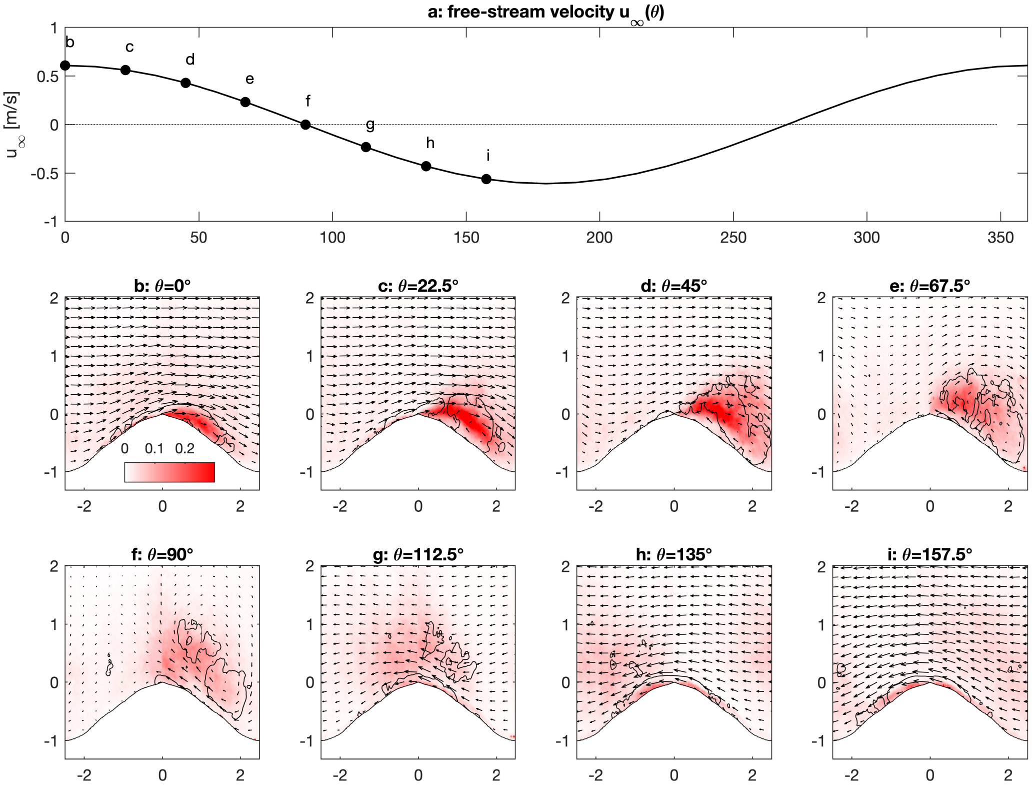

Figure 8. Turbulence intensity, e_{ti}, of the reference sinusoidal-flow test (SIN60a). In b-i, e_{ti} is normalized by $U^2_{\infty,1}$, and the solid contours indicate Λ^*_i=1. Both x and z coordinates are normalized by ripple height η.

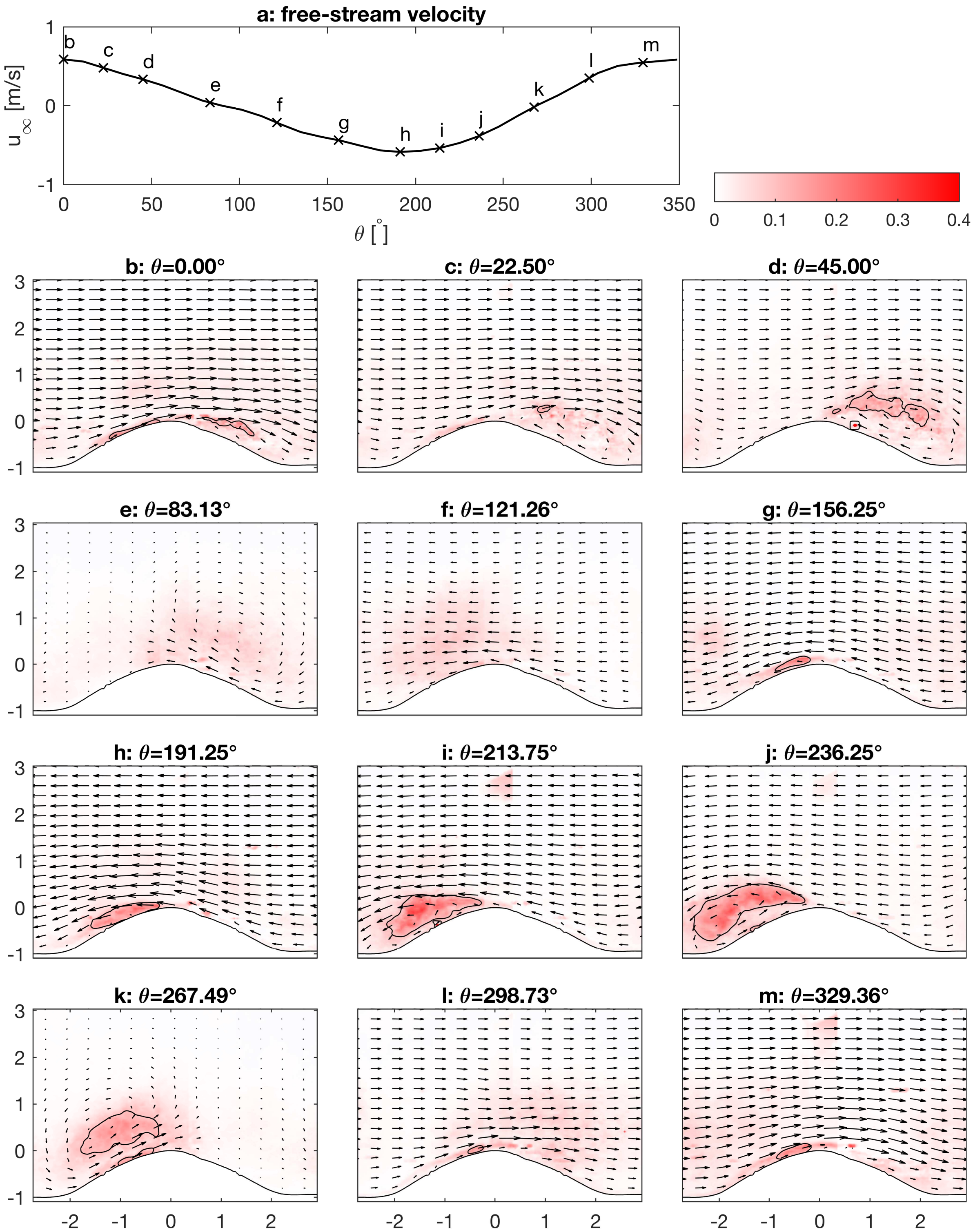

Figure 9. Turbulence intensity, e_{ti}, of test ASY60b. In b-m, e_{ti} is normalized as $e^*_{ti} = e_{ti}/U^2_{\infty,1}$, and the solid contours indicates e^*_{ti}=0.1. Both x and z coordinates are normalized by ripple height η. A moving average based on a 5-by-5 window is applied to reduce data noise.

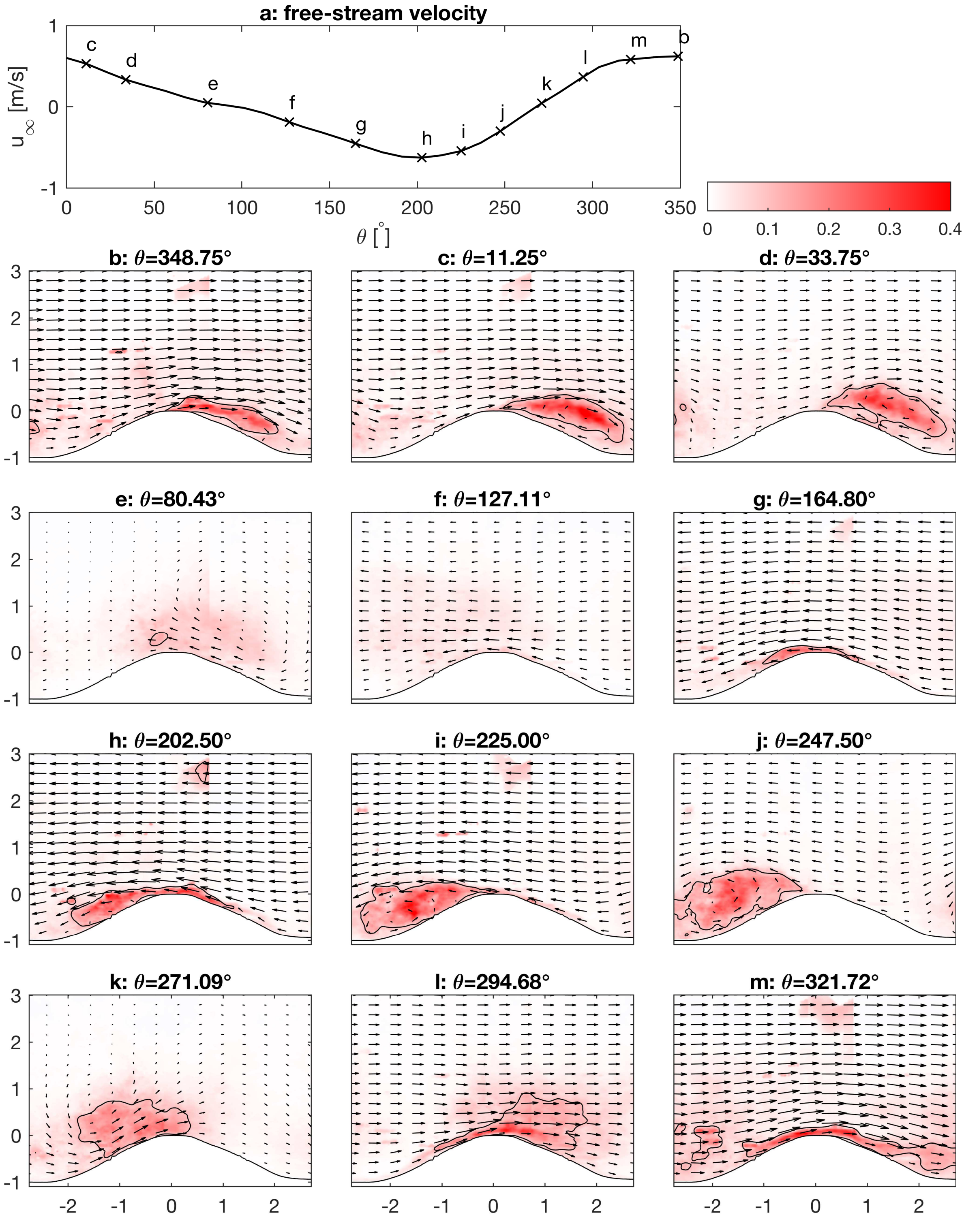

Figure 10. Turbulence intensity, e_{ti}, of test ASY60a (see the caption of figure 10 for descriptions.

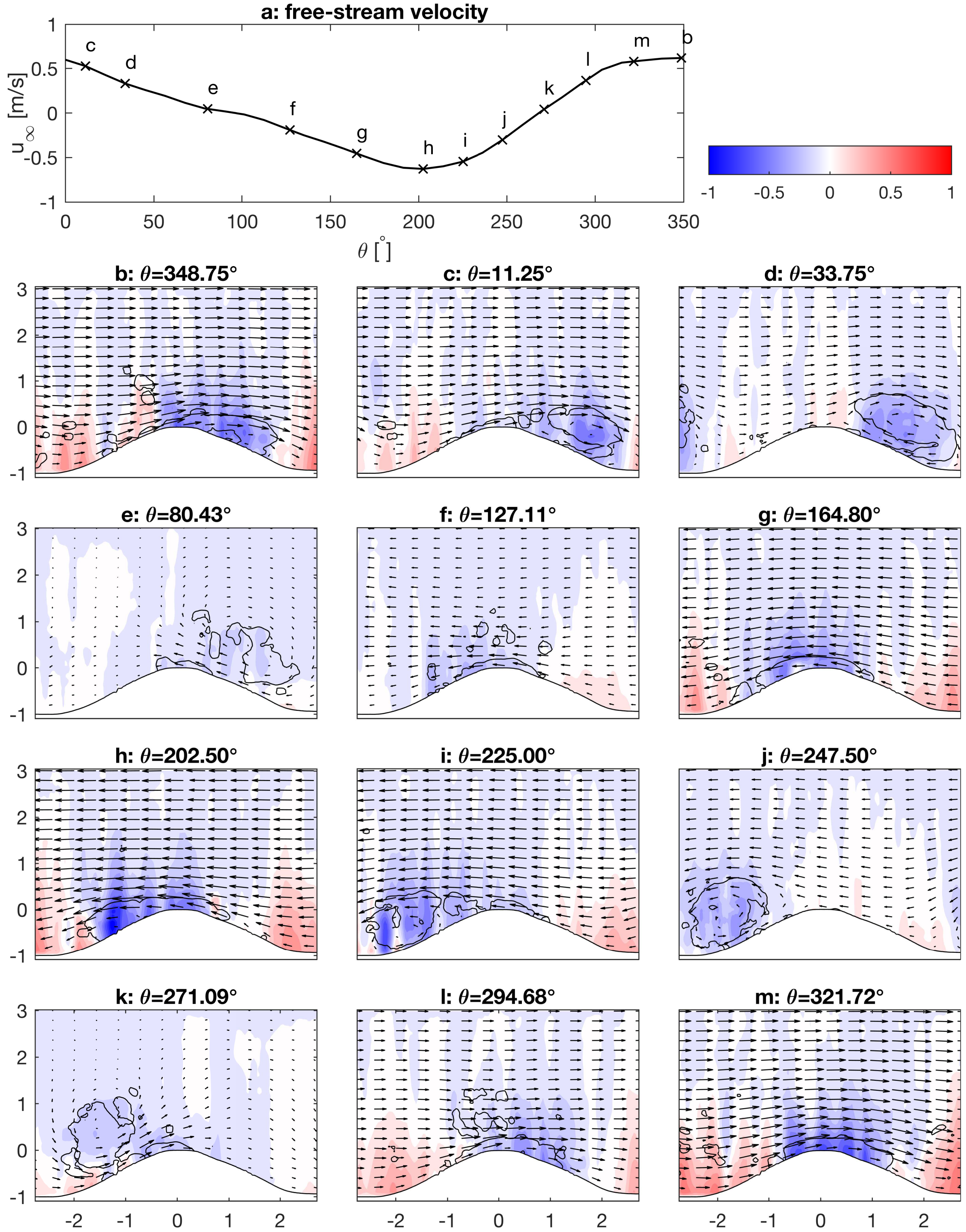

Figure 11. Spatial and temporal variation of phase-averaged pressure field for test ASY60a. The solid contours in b-m indicates $\Lambda_i^* = 1$. Both x and z coordinates are normalized by ripple height η. A moving average based on a 5-by-5 window is applied to reduce data noise.

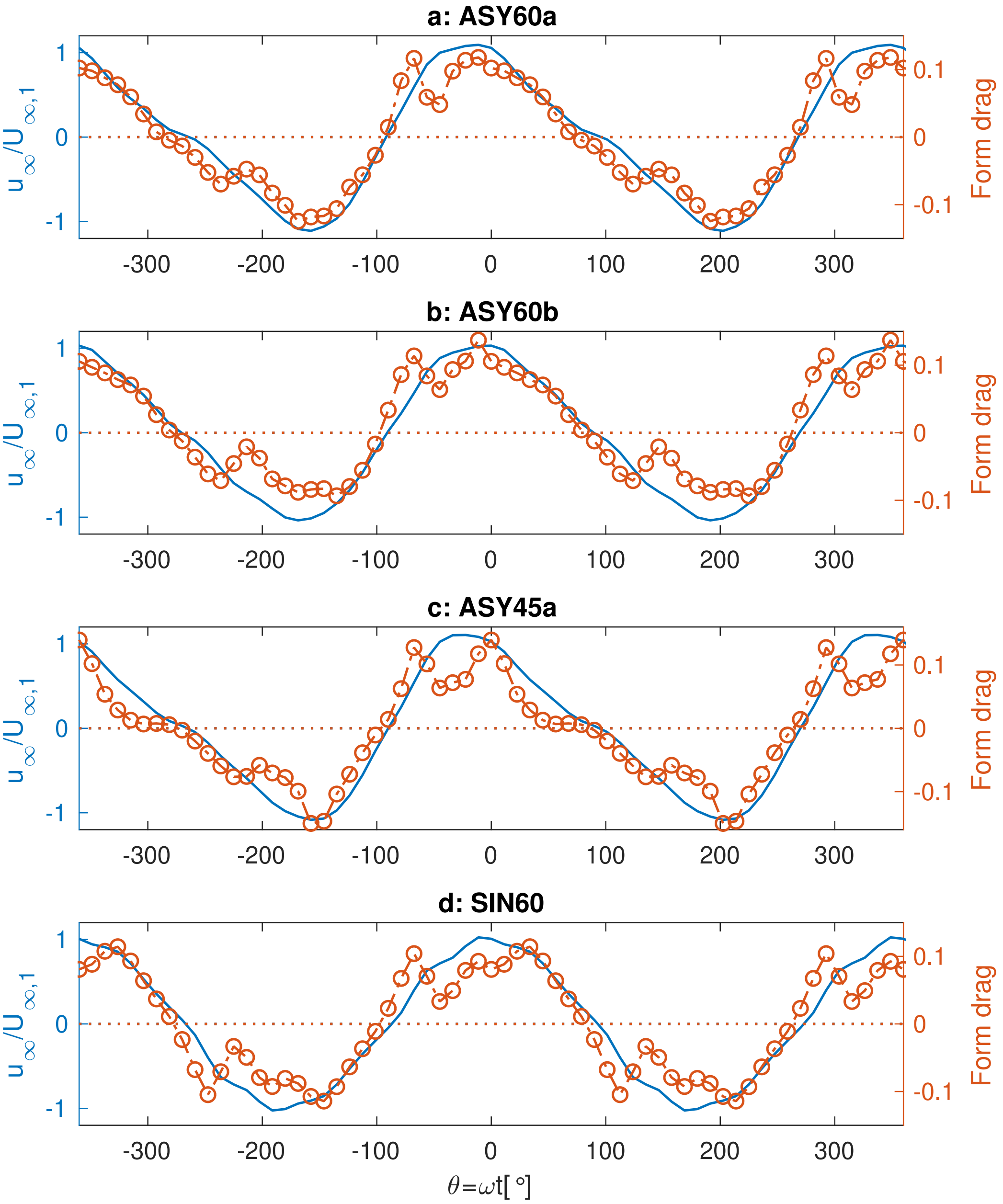

Figure 12. Normalized form drag.

Table 1. Test conditions

Test ID	$U_{\infty,1}$ [m/s]	$U_{\infty,2}/U_{\infty,1}$	Φ_2 [°]	T [s]	η [cm]	λ [cm]	η/λ	c_b [mm/s]
ASY60a	0.57	0.27	92.46	6.25	11.09	60.57	0.18	0.35
ASY45a	0.45	0.26	89.04	6.25	9.43	58.00	0.16	0.34
ASY60b	0.57	0.14	89.29	6.25	10.98	62.00	0.18	0.19
SIN60	0.61			6.25	12.00	59.67	0.20	